The spatial variability of the long-term sea surface temperature warming trend in the Japan Sea

松浦, 浩巳

出版情報：Kyushu University, 2024, 博士（理学）, 課程博士
バージョン：
権利関係：

The spatial variability of the long-term sea surface temperature warming trend in the Japan Sea

Hiromi Matsuura

Department of Earth System Science and Technology,

Interdisciplinary Graduate School of Engineering Sciences

Kyushu University

Abstract

The Japan Sea shows a significantly stronger long-term sea surface temperature (SST) warming trend compared to its surrounding seas. The SST warming trend is also associated with a non-uniform spatial pattern. A meridionally alternating zonal band structure exists with maximum and minimum patches on top. This study examines the mechanism behind the formation of this spatial variability from 1993 to 2019 using idealized models and satellite-based observation datasets.

Idealized models show that the combination of the Japan Sea Throughflow and atmospheric heating is the main process that generates the alternating zonal band structures. Eulerian heat budget analysis shows that the throughflow prevents gradual warming due to atmospheric heating along its path. Lagrangian particle tracking experiments show that a weak SST trend forms where the residence time is short, while a strong SST trend forms where the residence time is long. These results suggest that the accumulation time of surface heating is one of the key parameters that determine the spatial structure of the zonal band pattern in the Sea of Japan.

Satellite-based observation datasets show that the meridional shift of the SST front is partly behind the formation of the maximum and minimum patches. From 1993–2002 to 2010–2019, the SST front in the western (129.125-129.825°E), central (133.125-134.875°E), and eastern (135.125-138.125°E) Japan Sea shifts northward, southward, and southward, respectively, in line with the movement of the zonal jet. The SST warming trends are enhanced where the shift is northward, while moderate or weakened where the shift is southward. In the western and eastern regions, the SST front and jet shift gradually, whereas in the central region, the movement is highly variable due to the presence of a mesoscale eddy. Our analysis suggests that changes in the SST warming trend along the SST front are linked to circulation variability but follow a distinct mechanism in the central Japan Sea compared to the western and eastern regions.

Acknowledgement

I would like to express my deepest gratitude to Associate Professor Shinichiro Kida for his encouragement and continuous support throughout my studies. His practical suggestions have always guided the direction of both my research and this thesis. I am deeply thankful for his mentorship in fostering my growth as a research scientist. Three years is far too short a time to fully absorb his vast knowledge of physical oceanography, master numerical modeling techniques, and refine my ability to structure my thoughts.

I would also like to extend my appreciation to my committee. I am grateful to Professor Atsuhiko Isobe and Professor Yusuke Okazaki for their valuable and constructive feedback on this thesis. Professor Isobe consistently provided insightful comments during our lab meetings, while Professor Okazaki not only gave helpful feedback on this thesis but also on the SPRING program, broadening my research interests beyond physical oceanography.

I am equally thankful to Assistant Professor Katsuto Uehara. His advice greatly improved the finer details of my research. I would like to acknowledge the support of the secretaries, Ms. Mibuchi, Ms. Iida, Ms. Tanaka, and Ms. Mine, as well as technician Mr. Yufu, whose assistance allowed me to fully focus on my research. The daily conversations with my lab members made my research life both fulfilling and enjoyable.

Finally, I would like to express my heartfelt thanks to my family and friends for their emotional and financial support during the times when I doubted myself. Without their support, this thesis would not have been completed.

Contents

Chapter 1 General Introduction

1.1 The importance of sea surface temperature on Japan’s future climate

The Intergovernmental Panel on Climate Change (IPCC) Sixth Assessment Report (2021) states, "It is unequivocal that human influence has warmed the atmosphere, ocean, and land." By comparing atmospheric temperatures simulated under scenarios that account for only natural variability to those that include anthropogenic greenhouse gas emissions, the report shows that a long-term trend of increasing atmospheric temperature occurs only in the scenario with anthropogenic greenhouse gas emissions. The report emphasizes the importance of understanding how global warming, the primary driver of climate change, will impact the future environment globally and locally.

Significant progress has been made in recent decades toward understanding the impacts of global warming on future regional climate such as wet regions becoming wetter and dry regions becoming drier (Fujita et al., 2019). Many of these studies suggest that the boundary conditions used in models, such as sea surface temperature (SST), are critical for accurately interpreting model results. Shiogama et al. (2016) investigated record-breaking air temperature events by comparing large-ensemble model results driven by historical and non-warming climate forcings. They found that human activities have altered the occurrences of the annual coldest (warmest) daily minimum (maximum) temperatures and that the estimated anthropogenic impacts on these probabilities are sensitive to SST used in the models. Endo et al. (2017) investigated future precipitation changes and their uncertainty under a 4°C warmer climate using six different SST patterns in East Asia. Heavy precipitation and tropical cyclones are key to accessing future natural disaster risks. Endo et al. (2017) found that annual maximum daily precipitation increases throughout East Asia, with uncertainty strongly linked to the SST patterns used in the models.

Given its island geography, the SST of the Japan Sea significantly influences Japan’s weather. Takahashi et al. (2013) conducted sensitivity experiments to assess the impact of SST increases over the entire sea and found that precipitation along the coast of the Japan Sea increased by more than 6% $°C^{-1}$. Yamamoto and Hirose (2008) highlighted that reproducing mesoscale oceanic eddies in the assimilated SST led to mesoscale fluctuations in heat fluxes, improving model accuracy compared to observations. SSTs could also play an important role in Japan's future weather conditions. Japan is expected to suffer from more heavy snowfall, precipitation, and intense tropical cyclones. Kawase et al. (2016) found that the amount of snowfall was reduced in the 4 °C warmer scenario than in the pre-industrial climate, while the number of heavy snowfall events increased in central Japan. Yoshida et al. (2017) studied future changes in tropical cyclone activity and found that the occurrence of intense tropical cyclones is projected to increase over a broader area south of Japan, with uncertainties tied to future SST patterns.

Observations show that the seas surrounding Japan have experienced gradual warming from 1900 to 2020 (Japan Meteorologic Agency (JMA) 2020). According to the JMA report, the average rate of warming is 1.14 °C century^{-1} between 1900 and 2019, which far exceeds the global average of 0.55 °C century^{-1}. Among the seas surrounding Japan, the Japan Sea exhibits the strongest long-term warming trend and, therefore, warrants detailed examination.

The Japan Sea is often called "a world ocean in miniature" (Ichie 1984). As a semi-enclosed marginal sea located in the western North Pacific, the oceanic features, such as western boundary currents, overturning circulation, and the interaction between subtropical and subpolar waters, are analogous to those found in the world's larger oceans. Understanding the mechanisms driving long-term SST changes in the Japan Sea not only contributes to gaining insights into the impact of global warming on Japan's present and future climate but also broadens our understanding of how global warming affects oceanic processes on the basin scale.

1.2 Spatial variability of the SST in the Japan Sea

The Japan Sea is connected to its surrounding seas primarily through three straits: the Tsushima Strait, the Tsugaru Strait, and the Soya Strait (**Fig. 1a**). Warm water enters through the Tsushima Strait from the East China Sea, while cold water exits to the Pacific Ocean and Okhotsk Sea through the Tsugaru and Soya Straits, respectively. This water exchange system and related pathways is known as the Japan Sea Throughflow (Kida et al., 2016). Two distinct pathways of the Japan Sea Throughflow exist within the sea. One is the coastal branch that flows along the northern coast of Japan. The other is the offshore branch that follows the eastern coast of the Korean peninsula. This branch forms a zonal jet at 38°N (Ito et al., 2014), aligning with a strong SST front known as the Japan Sea subpolar front, where intense air-sea interactions occur (Park et al., 2004, 2007; Ohishi et al., 2019; Zhao et al., 2017).

The annual climatological SST field of the Japan Sea shows warm SST in the south and cold SST in the north with abrupt changes in SST at the Japan Sea subpolar front. The Japan Sea throughflow plays an important role in establishing this spatial pattern by bringing warm water to the southern region of this front, while local monsoonal winds cool the interior (Hirose et al., 1996). Hirose et al. (1996) show that the general heat balance occurs between the net lateral heat input from the ocean and surface cooling to the atmosphere. When the heat flux is estimated through the bulk method using observational data, the surface heat loss is about -53 W m^{-2}, balancing the net lateral heat flux induced by the exchange flows through the straits. This heat exchange system and pathways of currents cause the general SST gradient within the Japan Sea to become more meridional than zonal.

Research on the temporal variability of SST in the Japan Sea has advanced with the increase in direct measurements. Initial studies utilized data from coastal observatories; Watanabe et al. (1986) investigated the interannual variability of SST. They applied lag correlations and discovered that this variability, originating from SST changes in the East China Sea, is carried by the Tsushima Warm Current. Isoda (1994a) explored areas further into the interior along 134°E and identified a connection between decadal SST variability and the Tsushima Warm Current. Minobe et al. (2004) used gridded temperature data from the World Ocean Database and complex empirical orthogonal function analysis. They attributed interannual and decadal SST variability in the Japan Sea's interior to atmospheric fluctuations. More recently, satellite measurements have been utilized to examine spatial SST variabilities influenced by eddies and shifts in frontal locations (Park et al., 2004, 2007). Satellite measurements are also utilized to assess marine heat waves, which are prolonged anomalously warm seawater events. Wang et al. (2022) found that the yearly sum of marine heat wave intensity around the Japan Sea has increased dramatically and suggests the importance of oceanic dynamics, rather than atmospheric forcing.

With nearly 40 years of satellite-measured SST data and 100 years of in-situ data, it is now possible to estimate long-term trends globally. In recent years, the basic properties of intensity and spatial distribution of the long-term trends have gained significant interest. The northwest Pacific Ocean is identified as a hotspot for SST warming (Wu et al., 2020). As mentioned earlier, the Japan Sea exhibits the most significant warming among the seas surrounding Japan (JMA 2020). Taguchi et al. (2017) also show decadal variability in ocean heat content. However, studies investigating the spatial variations in the SST warming trend are still limited. Yeh et al. (2010) investigated long-term trends for over 100 years using an in-situ dataset with a spatial resolution of 1°×1°. They found a maximum warming trend in the south near the coast of Japan. Na et al. (2012) examined the long-term SST and heat content in the upper 300m and found that the long-term fluctuation of these two values was related to the upper ocean circulation, particularly the Tsushima Warm Current. Lee and Park (2019) analyzed temporal and spatial variations in SST trends using a finer resolution of 0.25°×0.25°. Their finding was that compared to the preceding 20 years (1980-2000), the intensity of the trend has decreased in the last 20 years (2000–2020). This change appears to be driven by fluctuations in the Arctic Oscillation index, aligning with Minobe et al. (2004)'s findings on decadal variability.

Lee and Park (2019) also found strong spatial differences within the Japan Sea, where they identified patches of maximum and minimum SST trends and a meridionally alternating zonal band structure. Zonal bands of weak trends exist around 36°N near the Tsushima Strait and around 40°N along the zonal jet. However, between these areas, along 38°N and 42°N, zonal bands of strong trends exist (**Fig. 1-1bc**). This alternating band structure observed in the annual SST trend reflects the SST trend during winter. The band structure becomes weak for summer, and an almost uniform SST trend appears. The magnitude of the SST trend also depends on the analysis period (see Figs. 6 and 7 of Lee and Park 2019). Lee and Park (2019) divided the analysis period into sections of 20 years, 1982 to 2018, and compared the spatial distribution of the SST trend. Their analysis shows that the magnitude of the SST warming trend has decreased in recent decades. Nevertheless, the zonal band structure remains consistent. Along the Japanese coast and at 40°N, a weak SST trend is observed. In the interior, a strong trend is observed.

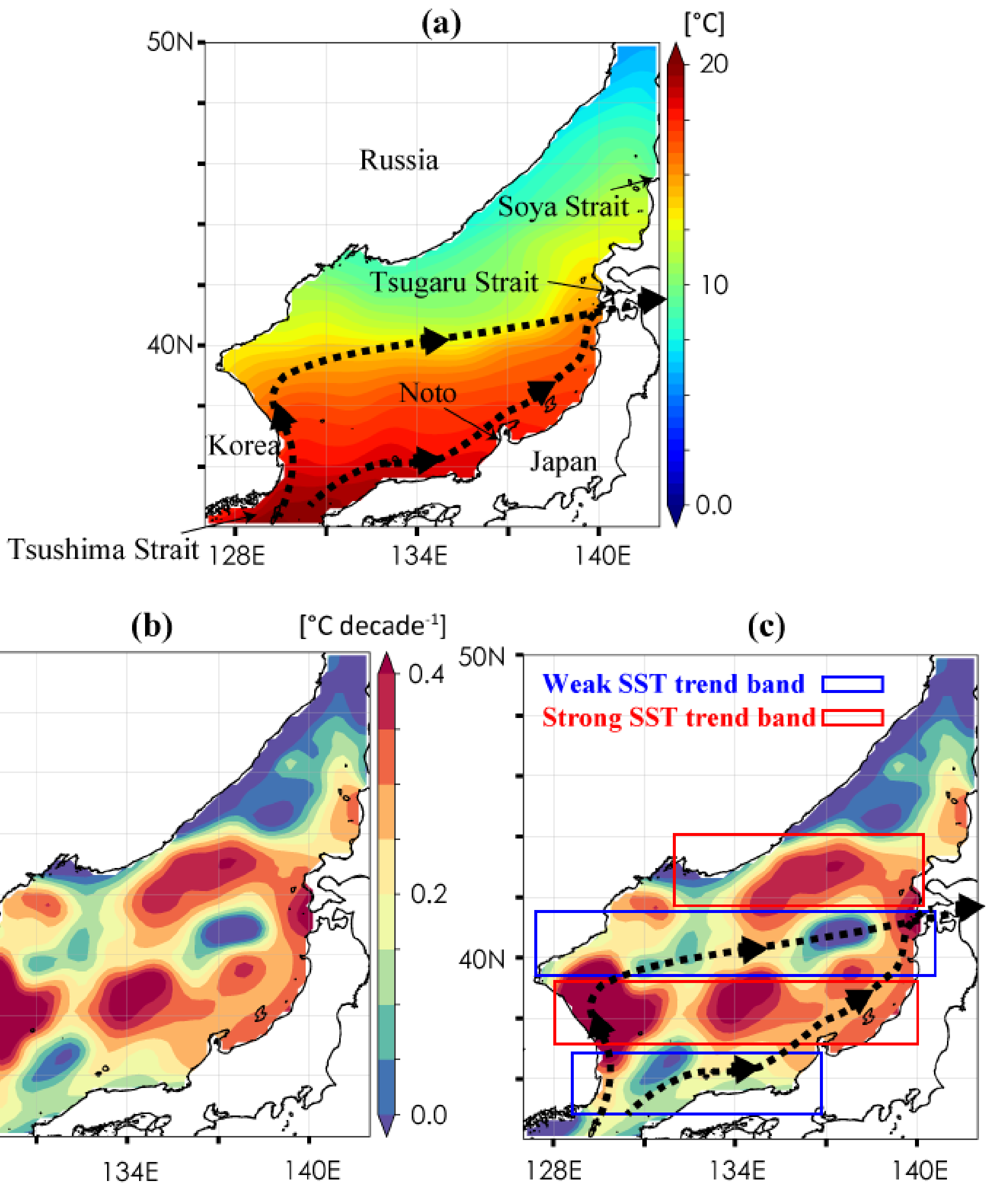

Figure 1-1. (a) Annual SST climatology with labeled geographic names. (b) SST trends observed from 1993 to 2019. (c) The meridional alternating band structures discussed in Chapter 2, with blue (red) boxes indicating regions of weak (strong) SST trends. The dashed arrows in (a) and (c) mark the typical path of the Japan Sea Throughflow. The Optimum Interpolation Sea Surface Temperature annual mean data from the Advanced Very High-Resolution Radiometer from 1993 to 2019 are used for those figures (Banzon et al., 2016). Figure 1 of Matsuura and Kida (2024).

What mechanisms create the spatial differences in the SST trend within the Japan Sea? JMA (2020) and Lee and Park (2019) examine the intensity of the spatially averaged trend and the characteristics of the spatial differences in the SST trends. However, the mechanism behind the formation of two major features remains unknown: the zonal band structure and maximum and minimum patches.

(a) For Zonal Band Structure: A Combination of atmospheric forcing with the Japan Sea Throughflow

We suggest that the formation of the zonal band structure is driven by a combination of atmospheric warming and cooling induced by the Japan Sea Throughflow. If the Japan Sea Throughflow rises SST by bringing in warmer water and the atmosphere weakens this heat input, a spatial pattern with warm zonal bands would be expected along its path. That pattern would likely show a significant warming trend near the Tsushima Strait, where the throughflow enters, as well as along the zonal jet at around 40 °N. However, the observed trends contradict this expectation, with a weaker SST trend band near the Tsushima Strait (**Fig. 1-1b**). In contrast, if cooler water is carried into the interior of the sea by the Throughflow, it would result in a weaker SST trend near the Tsushima Strait. This spatial pattern would be more consistent with observations. The atmospheric temperature around Japan has been warming in recent years (Kuroda et al., 2020; Kawase et al., 2023), so it can have a warming effect on the SST. These observations imply that relatively cool water is brought by the Japan Sea Throughflow compared to the water within the Japan Sea while heating is forced by the atmosphere.

The zonal band structure may also reflect the varying residence times of surface water. Water parcels directly on the path of the Throughflow travel from the Tsushima Strait to the Tsugaru and Soya Straits, whereas those in other areas remain within the sea. Consequently, the heating effect experienced by water parcels is reduced along the throughflow paths, resulting in a weaker SST trend along the Throughflow compared to other regions. Kodama et al. (2016) investigated the residence times of particles entering the Tsushima Strait, finding that the short residence time limited nitrate accumulation from atmospheric deposits over the Japan Sea (see Fig. 5 of Kodama et al., 2016).

(b) For Maximum and Minimum patches: Meridional Shift of the SST front

Internal variability, such as a meridional shift of the SST front, is suggested to explain the maximum and minimum patches within the zonal band structure. The SST front is located around 40°N and possesses the strongest meridional gradient of SST (Kida et al., 2015). If the position of the front gradually shifts to the north (south), the SST should show an increasing SST trend there because the warm (cool) water moves northward (southward). Studies show that the SST front is gradually shifting and that the shift is not in a monotonous direction but meandering (Park et al., 2007; Chen et al., 2022). These results support that maximum and minimum patches within the zonal band structure may be created by the meridional shift of the SST front with a meandering case. However, whether such changes in the SST front shift are related to the position of the jet, a zonal flow known to form along the subpolar front, is unclear.

1.3 Purpose and outline of the thesis

This study examines the mechanisms responsible for creating the observed spatial variability of SST trends in the Japan Sea. Chapter 2 investigates the role of atmospheric heating and the Japan Sea Throughflow in forming alternating zonal band structures. We use a numerical model with an idealized setup with a flat rectangular coastline. This approach enables us to identify the primary process. The impact of variation in bathymetry is then examined by using a model with realistic bathymetry. We also examine whether the Japan Sea Throughflow regulates the residence time and can create the alternating zonal band structure using a particle tracking model. In Chapter 3, we investigate the meridional shift of the SST front and the jet and examine their impacts on the maximum and minimum patches of the SST trend found within the zonal band structure. Chapter 4 presents conclusions and provides future research directions.

Chapter 2 SST response to atmospheric warming

2.1 Introduction

Observations indicate that atmospheric temperatures around Japan have been rising in recent years (Kuroda et al., 2020; Kawase et al., 2023), which can warm SST over the Japan Sea on a broad scale. The observed meridionally alternating zonal band structure may be attributed to the combined effects of atmospheric warming and the Japan Sea Throughflow, as the throughflow mitigates warming signals by regulating residence time in the sea along its path. To understand the fundamental process of atmospheric warming and the throughflow on the SST trend, we use an idealized model with a flat rectangular coastline, followed by a realistic bathymetry model to assess the impact of realistic bathymetric variations. Additionally, we develop a particle tracking model to estimate residence times. Model setup descriptions are provided in Section 2.2. Results from the idealized and realistic bathymetry models are presented in Sections 2.3 and 2.4, respectively. Differences in residence time caused by the Throughflow are also discussed using the particle tracking model in Section 2.4. Section 2.5 presents the conclusions of this chapter.

2.2 Method

2.2.1 Idealized flat rectangular coastline experiments

KINACO (Matsumura and Hasumi 2008) is used to create a numerical model with a rectangular basin, a flat bottom, and straight coastlines. We will use an idealized setup to understand the basic mechanism behind the formation of zonal band structures in the SST trend. A slowly evolving SST warming trend is forced through two steps. First is the spin-up stage. The model is forced by steady external forcings to reach a steady state. The second stage consists of two experiments with different surface heat fluxes (Q). A constant surface heat flux ($Q = \bar{Q}$) is used for one experiment, and an additional surface heat flux anomaly ($Q = \bar{Q} + Q'$) is used for the other experiment. The effect of atmospheric temperature warming is included in this second experiment. The mechanism underlying the SST trend will be examined by taking the differences between the two experiments.

2.2.1.1 Model Setup

The rectangular model domain is used to represent the Japan Sea with a horizontal resolution of 10 km. The domain is 1200 km in both meridional and zonal directions with a depth of 1000 m (**Fig. 2-1a**). There are two shallow straits, representing the Tsushima Strait at the southwest corner and the Tsugaru Strait at the middle of the eastern boundary, respectively. The depths of the straits are 100 m deep. For simplicity, flow through the Soya Strait is excluded. There are coastal shelf regions along the southern and eastern coastlines with a slope of 0.001. The shelf break is at 100 m depth, and the minimum depth along the coast is 20 m. These shelves connect the two straits. The coastal branch forms along this shelf due to the presence of topographic β (Kawabe 1982b; Yoon 1982). The vertical resolution varies with depth. For the upper 200 m, from 200 to 600 m, and 600 m to the bottom, the resolutions are 20 m, 40 m, and 80 m, respectively. The hydrostatic approximation is used.

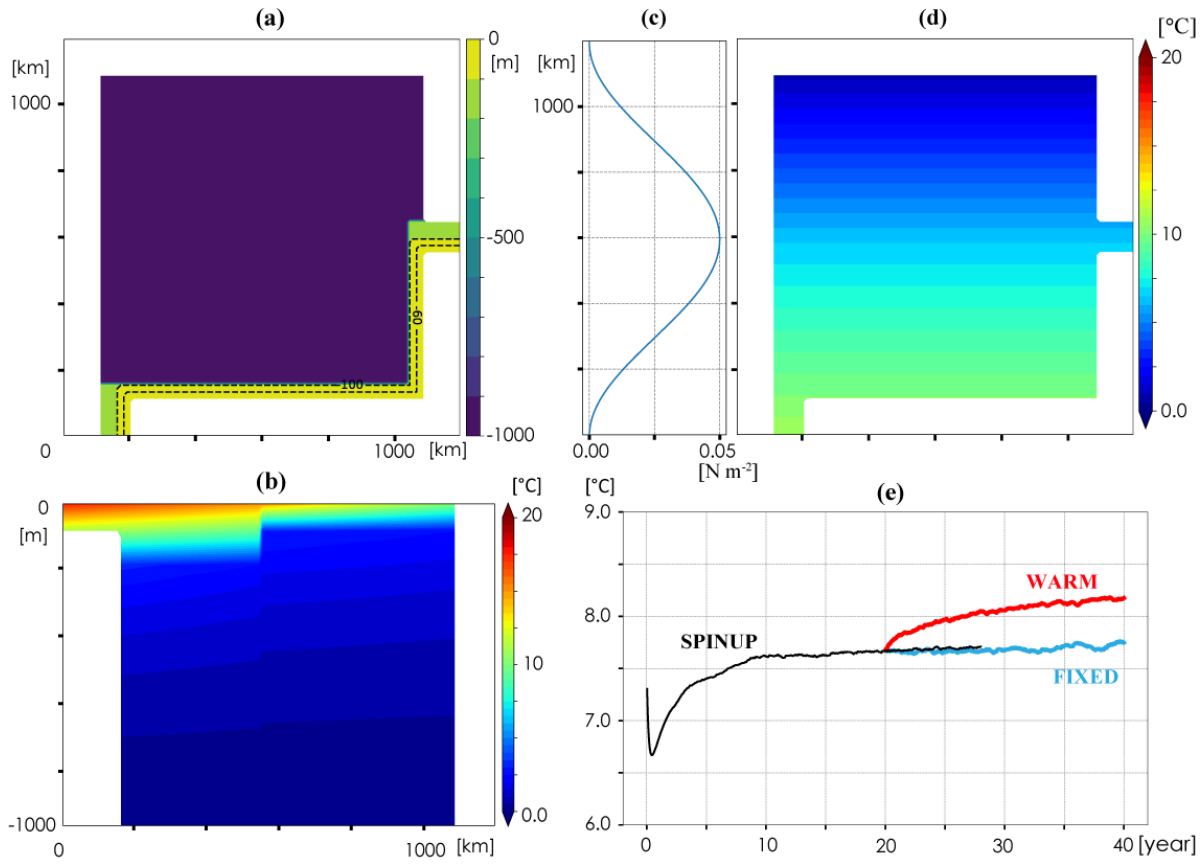

Figure 2-1. Idealized model settings: (a) Bathymetry with isobaths of the shallow shelf along the southern and eastern coastlines, represented by black dashed lines. (b) The vertical cross-section of the initial temperature at x = 200 km. (c) The surface wind stress profile. (d) The temperature profile used for restoring SST during SPINUP. (e) Time series of basin-averaged SSTs, with black, blue, and red lines showing the results of the SPINUP, FIXED, and WARM experiments, respectively. Figure 2 of Matsuura and Kida (2024).

The horizontal viscosity A_H and diffusivity K_H are constants, with a value of 100 $m^2\ s^{-1}$. Free slip is used for the lateral boundary condition. The vertical viscosity A_V and diffusivity K_V are estimated using the generic length-scale scheme (Umlauf and Burchard 2003). For bottom drag, a quadratic form is used with a coefficient of C_d = 0.055.

The initial temperature field is set based on the annual climatology of World Ocean Atlas (WOA) 2018 estimated using the period 2005–2017 (Locarnini et al., 2019). The depth of the thermocline is 200 m to the southern half and 100 m to the northern half. At the mid-basin (y = 600 km), a temperature front is located and represents the subpolar front (**Fig. 2-1b**). Density changes occur only due to temperature variations and salinity is set to a uniform value of 35.

The throughflow, with a constant volume transport of 2.2 Sv, is forced by an inflow through the southwestern strait and an outflow through the eastern strait. This magnitude is comparable to the observed value of the Tsushima Current during winter (Takikawa et al., 2004; Fukudome et al., 2010). The temperature profile of this inflow at the southern boundary is the same as that prescribed as the initial condition along this location. Even if the ocean interior changes over time, this value remains constant and ensures that the heat input is constant. The outflow temperature is determined by the temperature simulated at the eastern boundary, which varies over time.

For surface wind stress, only zonal wind stress is applied. The magnitude varies meridionally and has its maximum value at mid-basin (y = 600 km) (**Fig. 2-1c**):

$$\tau_x = 0.025\,cos\left(\frac{600 - y}{600}\pi\right) + 0.025 \qquad (2-1)$$

where y is in kilometers. The annual mean of the Japanese Ocean Flux Data Sets with Use of Remote-Sensing Observations (J-OFURO3) dataset (Tomita et al., 2019) is used for the maximum wind stress (0.05 N m^{-2}). Meridional wind stress is zero. The magnitude and spatial pattern of the wind stress remain constant throughout the model experiment, forcing a double-gyre circulation. A double-gyre circulation is a central component of the Japan Sea circulation system (Yoon et al., 2005; Kim et al., 2020).

An idealized March climatology is used to restore the model SST (**Fig. 2-1d**). March is chosen since it is the coldest month. The profile varies only in the meridional direction and is created based on 1981–2010 data from WOA 2018 (Locarnini et al., 2019). To avoid long-term drift in the SST during the spin-up stage, the model SST is restored with a time scale of 30 days instead of a prescribed surface heat flux. The magnitude of the wind stress does not affect the magnitude of surface heat flux.

After about 20 years of numerical integration, the upper-layer temperature of the model reaches a steady state. The model is then integrated for another 7 years (**Fig. 2-1e**). This experiment is hereafter referred to as SPINUP.

2.2.1.2 Warming SST experiment

As mentioned earlier, the mechanism of the warming SST trend is examined by conducting two experiments. The model is forced using a constant surface heat flux ($\bar{Q}$) in the first experiment, referred to as the FIXED experiment. Q is based on the average of the last 7 years of SPINUP. This experiment aims to produce an SST field with no long-term trend. The initial condition is set to the final day of the 20th year of SPINUP, and the experiment is integrated over 20 years. All settings other than the surface heat flux are set identically to those in SPINUP.

A warming trend is forced for the second experiment and will be referred to as WARM (**Fig. 2-1e**). The surface heat flux has an additional anomaly (Q') of 5 W m^{-2} on top of the FIXED experiment. This forcing will induce a warming trend in SST of approximately 0.21°C $decade^{-1}$, aligning with observed data. A positive value is used for downward heat flux. The anomalous heat flux is constant both temporally and spatially. It is also important to note that the sign of the total surface heat flux is still negative and acts to cool the SST ($\bar{Q} + Q' < 0$). The anomalous heat flux will mitigate the cooling effect of the surface heat flux used in the FIXED experiment. As described earlier, the temperature of the inflow at the southwestern strait remains unchanged, ensuring no anomalous heat is introduced through the straits. We will examine the difference between this experiment and FIXED for analyzing the SST trend.

2.2.2 Realistic coastline experiments

The impact of the Japan Sea's detailed bathymetry will be examined by conducting numerical experiments using ETOPO bathymetry data (Amante and Eakins 2009) (**Fig. 2-2a**). Hogan and Hurlburt (2000) show that bottom topographic features such as the Yamato Rise can influence the flow field. Three experiments are performed with surface heat fluxes forced identically to SPINUP, FIXED, and WARM experiments. The differences are the presence of realistic bathymetry, coastlines, and a wind stress profile. The zonal wind stress now has a maximum located at y = 670 km. These experiments will be referred to as R-SPINUP, R-FIXED, and R-WARM, respectively.

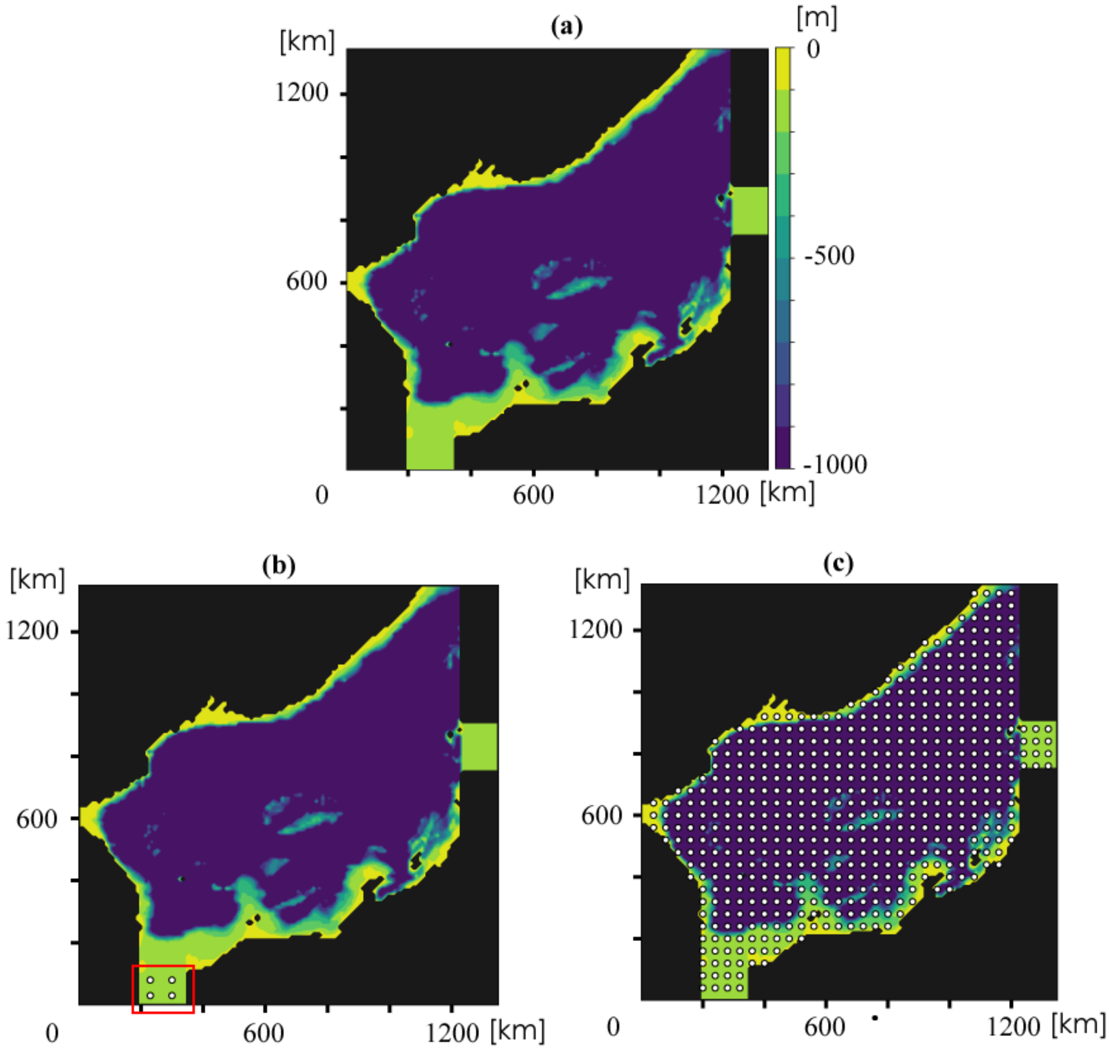

Figure 2-2. (a) The model configuration used for experiments with realistic coastlines. (b) The release locations of particles in P-TSUSHIMA (indicated by the red box) and (c) in P-AIR. Particles are displayed at a 40 km interval for clarity. Figure 3 of Matsuura and Kida (2024).

2.2.3 Heat budget analysis

The heat balance equation is used to investigate the mechanism responsible for creating the spatial differences in the SST trend:

$$\frac{\partial T}{\partial t} = -\nabla_H \cdot (\overrightarrow{u_H} T) - \frac{\partial}{\partial z}(wT) + K_H {\nabla_H}^2 T + K_V \frac{\partial^2 T}{\partial z^2} \qquad (2-2)$$

The tendency term is shown on the left side. The horizontal heat transport convergence, vertical heat transport convergence, horizontal diffusion, and vertical diffusion terms are on the right side. Vertical integration of Eq. 2-2 across the upper layer is:

$$\frac{\partial T_m}{\partial t} = \{-\nabla_H \cdot (\overrightarrow{u_H} T)\}_m + \frac{1}{H}(wT)|_{z=-H} + \{K_H {\nabla_H}^2 T\}_m + \{-\frac{K_V}{H}\frac{\partial T}{\partial z}|_{z=-H}\} + \frac{Q}{\rho_0 C_p H} \qquad (2-3)$$

where ρ_0 is the seawater density, C_p the specific heat at constant pressure, Q the surface heat flux, and H the depth of the upper-layer set to 200 m. For regions where shallower than 200 m, the actual bottom depth is used. Bracketed variables are vertically averages over 200 m. We will hereafter refer to the SST by T_m , the vertically averaged temperature:

$$T_m = \frac{1}{H}\int_{-H}^{0} T\, dz$$

Then we divide each term of Eq. 2-3 (A) into steady ($\bar{A}$) and trend (A') components:

$$A = \bar{A} + A'$$

where $\bar{A}$ represents FIXED and A' is the difference between WARM and FIXED. For FIXED, the heat balance equation can be expressed as:

$$0 = \overline{\{-\nabla_H \cdot (\overrightarrow{u_H} T)\}_m} + \overline{\{\frac{1}{H}(wT)|_{z=-H}\}} + \overline{\{K_H {\nabla_H}^2 T\}_m} + \overline{\{-\frac{K_V}{H}\frac{\partial T}{\partial z}|_{z=-H}\}} + \frac{\bar{Q}}{\rho_0 C_p H} \qquad (2-4)$$

The first two terms on the right are time means of horizontal and vertical heat transport convergence. The latter three terms are horizontal and vertical diffusion and surface heat flux. For WARM, the heat balance equation expresses the SST trend:

$$\frac{\partial T_m{}'}{\partial t} = \{-\nabla_H \cdot (\overrightarrow{u_H} T)\}_m{}' + \{\frac{1}{H}(wT)|_{z=-H}\}' + \{K_H \nabla_H{}^2 T\}_m{}' + \{-\frac{K_V}{H}\frac{\partial T}{\partial z}|_{z=-H}\}' + \frac{Q'}{\rho_0 C_p H} \quad (2-5)$$

The term on the left is the SST trend (ST) term. The first two terms on the right are the anomalous horizontal heat transport convergence (HH) and anomalous vertical heat transport convergence (VH) terms. The latter three terms are anomalous horizontal diffusion (HDIF), anomalous vertical diffusion (VDIF), and anomalous surface heat flux (SH) terms. The mechanism behind the SST trend will be examined by using Eq. 2-5 based on the spatial averages of each term that represents the coastal branch, offshore branch, southern interior, and northern gyre. We will define the exact location of these four regions in WARM and R-WARM separately for each experiment since they depend on the flow field.

2.2.4 Residence time

Two particle tracking experiments are conducted using R-WARM to assess the residence time of water parcels within the Japan Sea. The first experiment, referred to as P-TSUSHIMA, releases particles at the Tsushima Strait at the southwest corner and examines its residence time (**Fig. 2-2b**). The second experiment, called P-AIR, releases particles in the interior of the Japan Sea and evaluates the residence time of water parcels influenced by surface heat flux (**Fig. 2-2c**). The residence time of water parcels is estimated such that they accumulate age as long as they remain within the model domain. The detailed methods for estimating residence time in each experiment are described below. The motion of the particles depends on the flow and random walk that represent diffusion. Once the particles are released, they move only in the horizontal direction and remain at the same depth. To examine the difference in flow at different depths, we will release particles at depths of 50 m and 90 m.

(a) P-TSUSHIMA

3000 particles are released from the Tsushima Strait on the first day of each year, beginning from year 20. When we assume that the distance from the Tsushima Strait to the Tsugaru Strait is 1200–1500 km and that the flow speed is 0.1 m s^{-1}, the estimated time for a parcel to travel between the two straits is approximately 120–150 days. Therefore, the residence time of particles released from the Tsushima Strait is expected to be less than one year as long as they remain along the throughflow path. We calculate the 20-year average distribution of particles at the end of each year. Exponential fitting is then applied to the profile showing age and the number of particles that remain along the throughflow path to estimate the decay time scale of particles. This fitted result is referred to as the residence time of Tsushima Strait water parcels.

(b) P-AIR

Particles are released every 10 km, with 8848 particles at a depth of 50 m and 8587 particles at a depth of 90 m at the start of each year, beginning in year 20. We anticipate that some particles will remain within the sea significantly longer than those following the throughflow. Starting from year 30, the 10-year average is calculated for the residence time estimated at the end of each year. We will consider particles released only within the last 10 years and derive the spatial means of particle numbers at a horizontal resolution of 10 km.

2.3 Idealized flat rectangular coastline experiments

2.3.1 Mean field

The time-averaged SST of FIXED shows warmer SST in the southern half of the model domain (**Fig. 2-3a**). This is because warm water enters from the southwestern strait. In contrast, a cold SST region develops in the northern half of the domain. A thick warm layer develops in the south, and a strong temperature gradient forms at y = 600 km (**Fig. 2-3b**). The time-averaged flow field of FIXED shows coastal and offshore branches. The surface flow starts bifurcating in the southwestern strait, where abrupt depth change exists. The coastal branch follows the southern and eastern coastlines and finally reaches the eastern strait. The offshore branch forms a western boundary current and detaches at the latitude of the eastern strait to form a zonal jet. This zonal jet is associated with an SST front. In the northern half of the domain, a cyclonic gyre forms, suggesting a wind-driven flow. Warm water is advected cyclonically and features a southward western boundary current.

The time-averaged heat balance (Eq. 2-4) indicates that heat is introduced by inflow from the southwestern strait, which bifurcates along the southern and western coastlines (**Fig. 2-3c**). Diffusion effects are limited to narrow regions such as the shelf break and the western boundary (**Fig. 2-3d**). Surface heat flux cools the SST (**Fig. 2-3e**) and is key in balancing heat transport convergence.

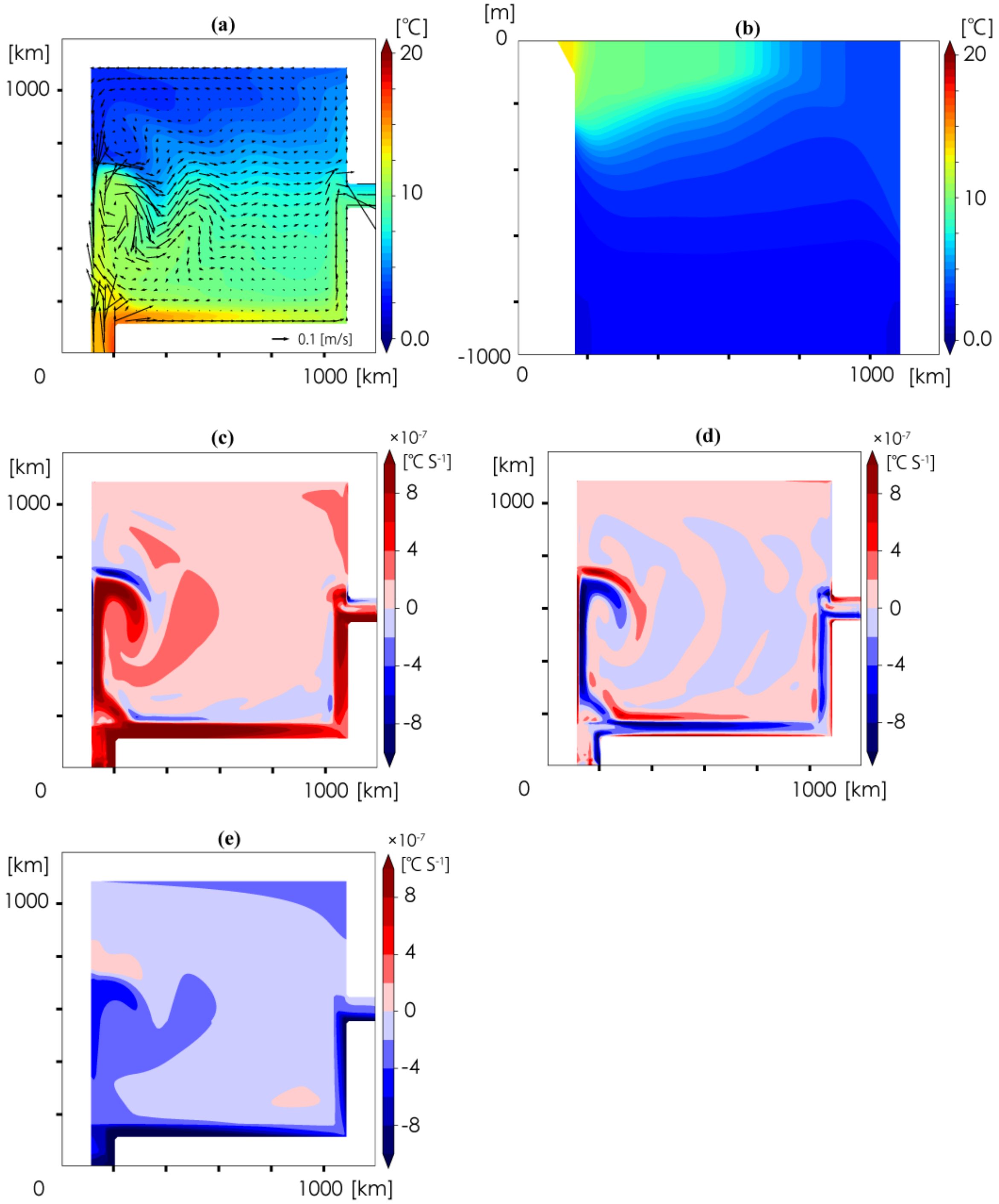

Figure 2-3. Time-averaged results: (a) The SST and flow field, and (b) the vertical temperature cross-section at x = 600 km, derived from the FIXED experiment during years 20 to 40. The terms from the time-averaged heat budget equation (Eq. 2-4) for the FIXED experiment: (c) The combined horizontal and vertical heat transport convergence, (d) the sum of horizontal and vertical diffusion, and (e) the surface heat flux. Figure 4 of Matsuura and Kida (2024).

2.3.2 SST trend

The spatially averaged SST trend induced in the WARM experiment is approximately 0.19 °C decade^{-1}. The experiment successfully simulates a meridionally alternating zonal band structure found in the observations (**Fig. 2-4a**). Here, our analysis focuses on four regions: coastal branch, offshore branch, southern interior, and northern gyre. The coastal branch is where the depth is shallower than 100 m. All regions have a zonal extent of 250 km (from x = 600 to 850 km) and a meridional width of 50 km. The size of each area remains the same. The fundamental heat balance remains qualitatively unchanged even if the size differs, provided that areas with abrupt depth changes are excluded.

The weakest SST trend is simulated in the coastal branch, with the signal gradually intensifying as it approaches the eastern strait, reflecting heat accumulation driven by anomalous surface heat flux. A weak SST trend is also present along the offshore branch. In the southern interior, a region of moderate SST warming, with magnitudes ranging from 0.1 to 0.2 °C decade^{-1}, is identified. The warming signal is also robust toward the east. This SST trend pattern differs from observations, where a stronger trend exists in the west. The difference may result from significant fluctuations near the western boundary's separation point, where the flow transitions into a zonal jet. This possibility is discussed in Section 4. A pronounced warming trend of 0.3 °C decade^{-1} in the northern gyre is noted where the throughflow is absent, and the wind stress curl primarily drives the circulation.

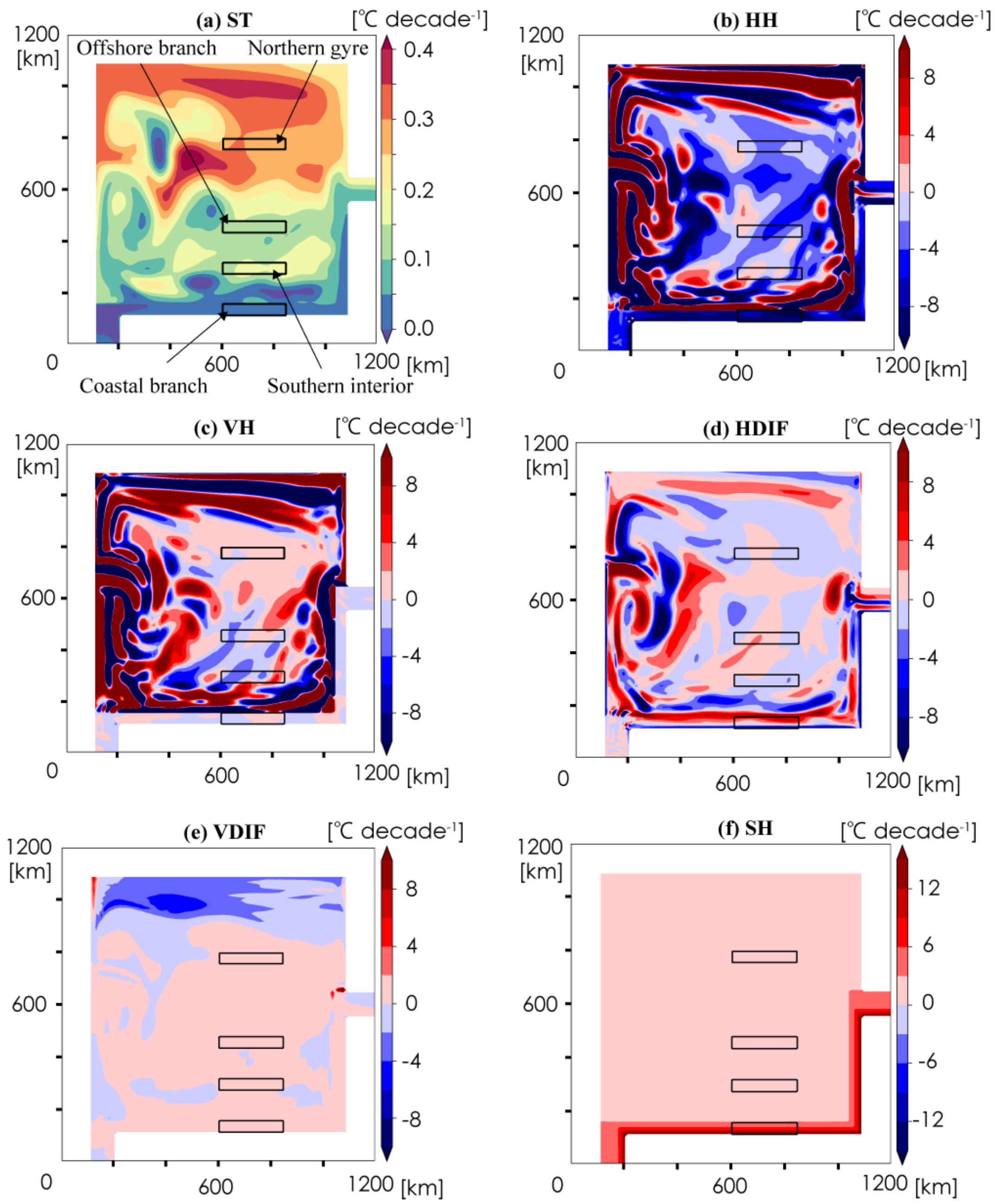

Figure 2-4. The terms from the SST trend equation (Eq. 2-5) for the WARM experiment are as follows: (a) ST, (b) HH, (c) VH, (d) HDIF, (e) VDIF, and (f) SH. Black contours mark the boundaries of the regions used for areal averaging, while black arrows indicate the names of each region. Figure 5 of Matsuura and Kida (2024).

2.3.3 Heat Budget of the SST trend

To understand the processes governing the SST trend in the WARM experiment, we will analyze the terms in the SST trend equation (Eq. 2-5). Since this subsection focuses specifically on SST trends rather than the mean state, the term “anomalous” will not be used in the discussion of Eq. 2-5 hereafter.

All four regions (coastal branch, offshore branch, southern interior, and northern gyre) indicate, to the first approximation, a similar balance. It is primarily between horizontal heat transport convergence and surface heat flux (**Fig. 2-5a-d**). The magnitudes of the horizontal and vertical diffusion terms are small. Significant temporal variability in flow is simulated near the boundaries and at the edge of the slope. Therefore the horizontal and vertical heat transport convergence terms exhibit strong fluctuations (**Fig. 2-4c,d**).

The two dominant terms within the coastal branch are horizontal heat transport convergence and surface heat flux (**Fig. 2-5a**). The contributions of vertical heat transport convergence and horizontal and vertical diffusion are almost negligible. The analysis indicates that the warming induced by surface heat flux is mitigated by the advection of relatively cold water from the southwestern strait. The surface heat flux in the coastal region is particularly significant compared to other areas, largely due to the limited water column thickness, which is constrained to 100 m or less by the slope.

Within the offshore branch, the surface heat flux is offset by cooling from horizontal heat transport convergence, similar to that of the coastal branch (**Fig. 2-5b**). Vertical heat transport convergence is negative, but its influence is weaker than horizontal heat transport convergence. Note that negative vertical heat transport indicates the downwelling of warmer upper-layer water since the sign of vertical heat transport convergence in Eq. 2-5 is expressed in heat transport terms and thus depends on the sign of vertical velocity. Horizontal diffusion has a positive impact, allowing heat from the warmer SST trends in the southern interior and northern gyre to diffuse into the offshore branch. Vertical diffusion also has a positive impact, reducing vertical heat loss. These positive contributions from horizontal and vertical diffusion lead to a stronger increase in SST trends in the offshore branch compared to the coastal branch.

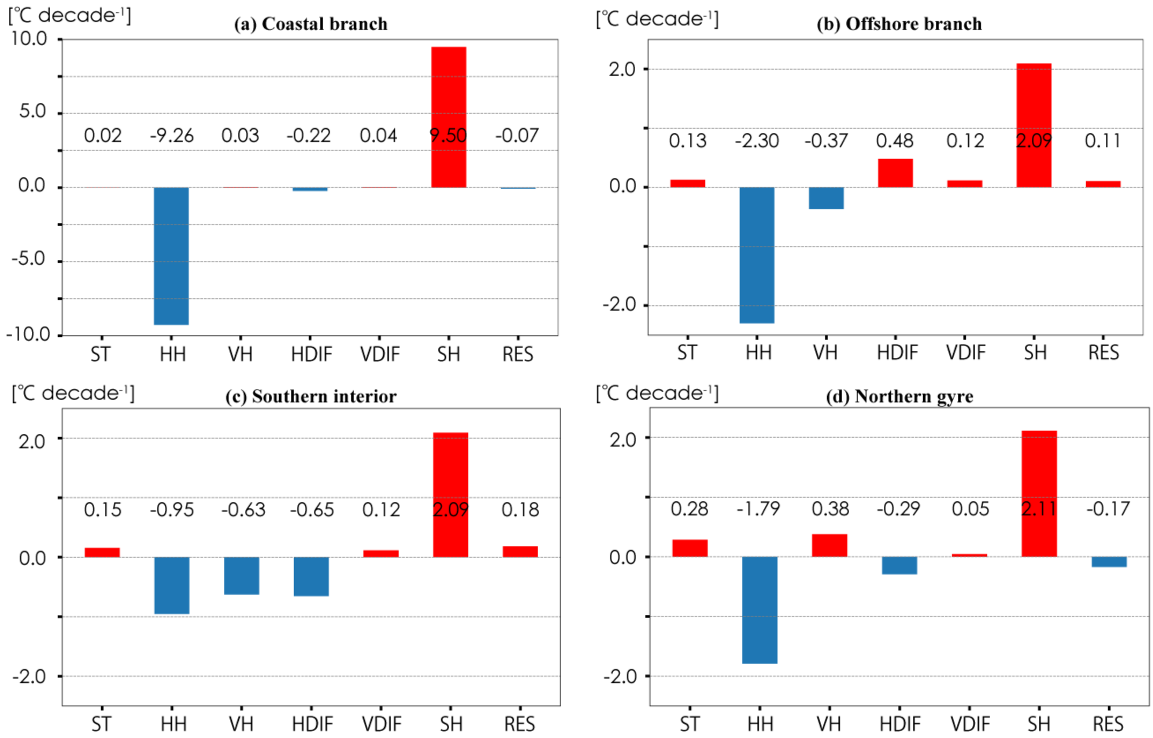

Figure 2-5. Spatial averages of ST, HH, VH, HDIF, VDIF, and SH from Eq. 2-5 are presented for the following regions: (a) coastal branch, (b) offshore branch, (c) southern interior, and (d) northern gyre. The RHS represents the residual. Red (blue) bars represent warming (cooling). Figure 6 of Matsuura and Kida (2024).

In the southern interior, a decrease in horizontal heat transport convergence results in a stronger warming trend compared to the coastal and offshore regions (**Fig. 2-5c**). While horizontal heat transport convergence remains negative, its magnitude is significantly reduced. This result is consistent with the low flow speed observed in the region. Because heat diffuses to the surrounding areas with weaker SST trends, we find the horizontal diffusion term to be negative with a magnitude comparable to horizontal heat transport convergence. Vertical heat transport convergence and vertical diffusion exhibit similar signs to those found in the offshore branch.

In the northern gyre, the horizontal heat transport convergence is lower than in the coastal and offshore branches (**Fig. 2-5d**), indicating that horizontal flow plays a less significant role there. However, this term is larger than the southern interior, possibly due to the stronger flow. The SST trend becomes stronger in the northern gyre than in the southern interior since the vertical heat transport convergence is positive and horizontal diffusion weakens. The vertical diffusion term remains positive, and this value is slightly smaller than that in the southern interior region. A positive vertical heat transport convergence term represents the upwelling of warmer upper-layer water. In the northern half of the domain, such a process is likely driven by Ekman upwelling that is induced by the wind.

Based on the heat budget analysis, we find the varying influence of horizontal heat transport convergence to be the key driver behind the formation of the zonal band structure in the SST warming trend. The flows along the coastal and offshore branches have zonal structures, which can successfully explain the impact of horizontal heat transport compared to the southern interior and the northern gyre. SST is uniformly warmed by the surface heat flux over the whole model domain and thus cannot create a zonal structure. The inability to explain the zonal band structure also applies to vertical heat transport convergence and diffusion.

2.3.4 Sensitivity to the trend in the flow field

The flow field trend in the WARM experiment could also influence the SST trend. The most significant changes in the flow field are simulated near the separation point of the western boundary current, where a weakening of the eastward zonal jet is detected, accompanied by eddy-like features (**Fig. 2-6**). These features may affect the SST trend around the jet (**Fig. 2-4a**). However, since most flow variations occur along the SST trend contours, the direct impact of the trend in the flow field on the SST trend is limited. The magnitude of the trend in the flow field is an order of magnitude smaller than that of the mean current, which is less than 0.01 m s^{-1} $decade^{-1}$.

The significance of the flow field in determining the spatial distribution of the SST trend was shown using the idealized flat rectangular coastline model. However, some discrepancies with observations remain, such as a trend that strengthens towards the west and a strong SST trend in the southern interior region with patches of maxima (**Fig. 1-1b**). The impact of realistic coastline and bathymetry settings on these factors will be explored in Section 4.

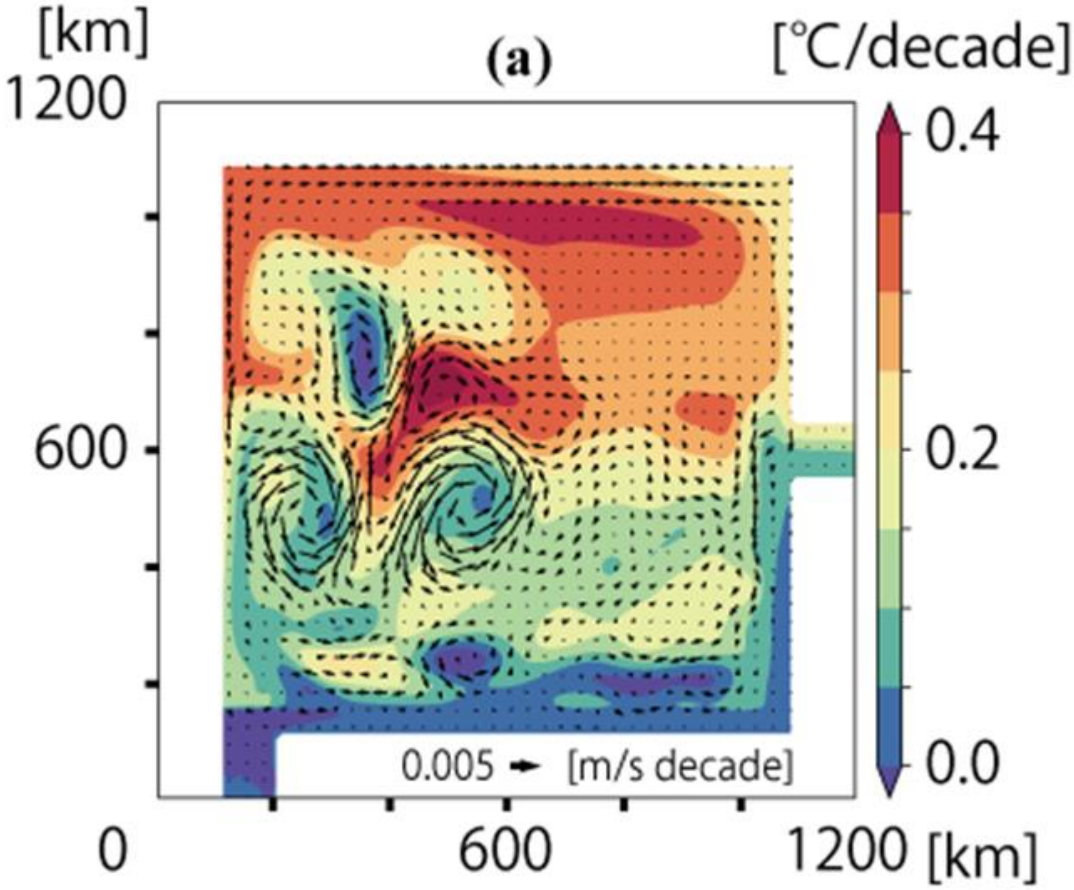

Figure 2-6. Trends in the flow field for the R-WARM experiment. Black arrows show the magnitude and the direction of the trends, and the color contours show SST trends. Figure S1 of Matsuura and Kida (2024)

2.4 Realistic coastline experiments

2.4.1 Mean Field

The R-FIXED experiment shows a mean SST field that closely resembles the FIXED experiment (**Fig. 2-7a**). A warm SST region is established near the Tsushima Strait that generally cools towards the north. A typical Japan Sea Throughflow pattern, with the inflow bifurcating into coastal and offshore branches, is also established in the mean flow field. North of the Noto Peninsula, the coastal branch becomes more diffused, making the shelf flow along the northern coast of Japan more discontinuous. The offshore branch follows a zonal path along the SST front and appears more stable than in the FIXED experiment. The western boundary current separates around y = 670 km, aligning with the position of the idealized wind stress curl zero. Southeast of this separation point, an anticyclonic recirculation gyre is present. The separation is located further north compared to observations, indicating overshooting, which will be discussed in the next section regarding its impact on the SST trend. The flow field is weak in the north of the offshore branch.

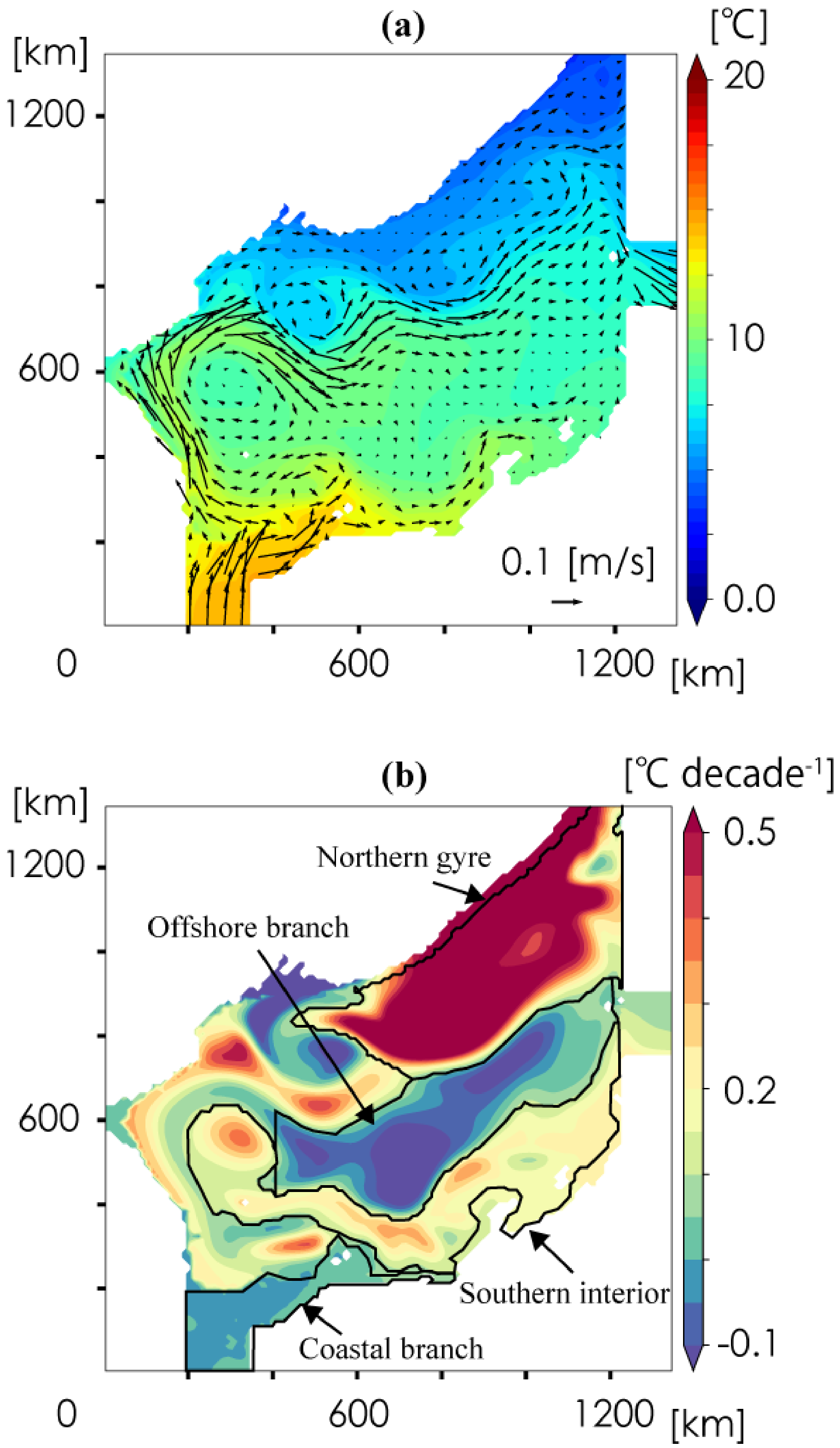

Figure 2-7. (a) Long-term averages of SST and the flow field for R-FIXED during years 20–40. (b) SST warming trend for R-WARM over the same period. Black contours represent the regions used for heat budget analysis: the coastal branch, southern interior, offshore branch, and northern gyre. Figure 7 of Matsuura and Kida (2024).

2.4.2 SST trend

The R-WARM experiment simulates a meridionally alternating zonal band structure (**Fig. 2-7b**) that closely resembles the observed pattern (**Fig. 1-1b**) as well as the results from the WARM experiment (**Fig. 2-4a**). Near the Tsushima Strait (y = 200 km) and the zonal jet (y = 600 km), weak SST trends are simulated. To the south (y = 400 km) and north (y = 800 km) of the zonal jet, stronger SST trends are present. We will define the coastal branch as the region with a depth of 200 m or less, where the SST trend magnitude is below 0.1°C decade^{-1} threshold (**Fig. 2-7b**). The offshore branch is defined as the region where the magnitudes of the SST trend are less than this threshold. The southern interior is defined where it is greater than the threshold. The northern gyre is defined as the region north of the zonal jet where the SST trend exceeds the threshold. To focus on processes in areas away from the slope, areas shallower than 200 m are excluded.

A region with a strong SST trend that exceeds 0.25 °C decade^{-1} is found east of the Noto Peninsula. The region is where the flow along the Japanese coast becomes discontinuous and is where we find the main difference between the R-WARM and WARM experiments. The SST trend also intensifies towards the west, as the separation point in R-WARM is significantly more stable than WARM since a stable recirculation gyre is established. We also find that regions with weaker SST trends are generally associated with where mean current speeds are greater than 0.04 m s^{-1}.

2.4.3 Heat budget of the SST trend

Each of the terms of the SST trend equation (Eq. 2-5) is now examined to understand the basic process behind the SST warming. This subsection focuses on the trend, similar to subsection 3.3, so the terms of Eq. 2-5 will be discussed here without using the term "anomalous".

In the coastal branch, the main balance is between the cooling due to horizontal heat transport convergence and the warming caused by surface heat flux (**Fig. 2-8a**). The diffusion terms are small. For a weak SST trend region to be established near the Tsushima Strait, the advection of water with a lower SST trend than the interior is crucial.

In the offshore branch, the basic balance is between the horizontal heat transport convergence and the surface heat flux (**Fig. 2-8b**). Here, the surface warming caused by surface heat flux is outweighed by the effect of horizontal heat transport convergence, and a lower SST trend is established. A positive vertical heat transport convergence term is found, likely due to the inclusion of areas with Ekman upwelling in the offshore branch.

In the southern interior, the heat transport convergence terms are larger compared to those in the offshore branch for both horizontal and vertical (**Fig. 2-8c**). The fluctuation of the currents near Japan's northern coast is likely responsible since these two terms largely cancel each other out. The total of combined horizontal and vertical heat transport convergences is smaller (-1.66 °C decade^{-1}) than those in the coastal (-4.11 °C decade^{-1}) or offshore (-1.96 °C decade^{-1}) branches. The relatively small magnitude of combined heat transport convergences in the southern interior indicates the overall influence of the flow field is weak. The difference in the combined horizontal and vertical heat transport convergences between the offshore branch and the southern interior is approximately 0.3 °C decade^{-1}, which is the main factor driving the increase in the SST trend from - 0.04 °C decade^{-1} in the offshore branch to 0.19 °C decade^{-1} in the southern interior.

In the northern gyre, the dominant factors affecting the heat budget are horizontal and vertical heat transport convergences and surface heat flux (**Fig. 2-8d**). The contributions from horizontal and vertical diffusion are minimal. Similar to the southern interior, the sum of horizontal and vertical heat transport convergences in the northern gyre is -1.26 °C decade^{-1}, smaller than the corresponding values in the coastal or offshore branches.

Within the coastal and offshore branches, the heat budget analysis indicates a significant influence from horizontal heat transport convergence. The presence of this term is what prevents SST warming, such as in the WARM experiment. There is notable compensation between horizontal and vertical heat transport convergences for the southern interior and the northern gyre, so the flow field has a weaker impact, contributing to a stronger SST trend than other regions.

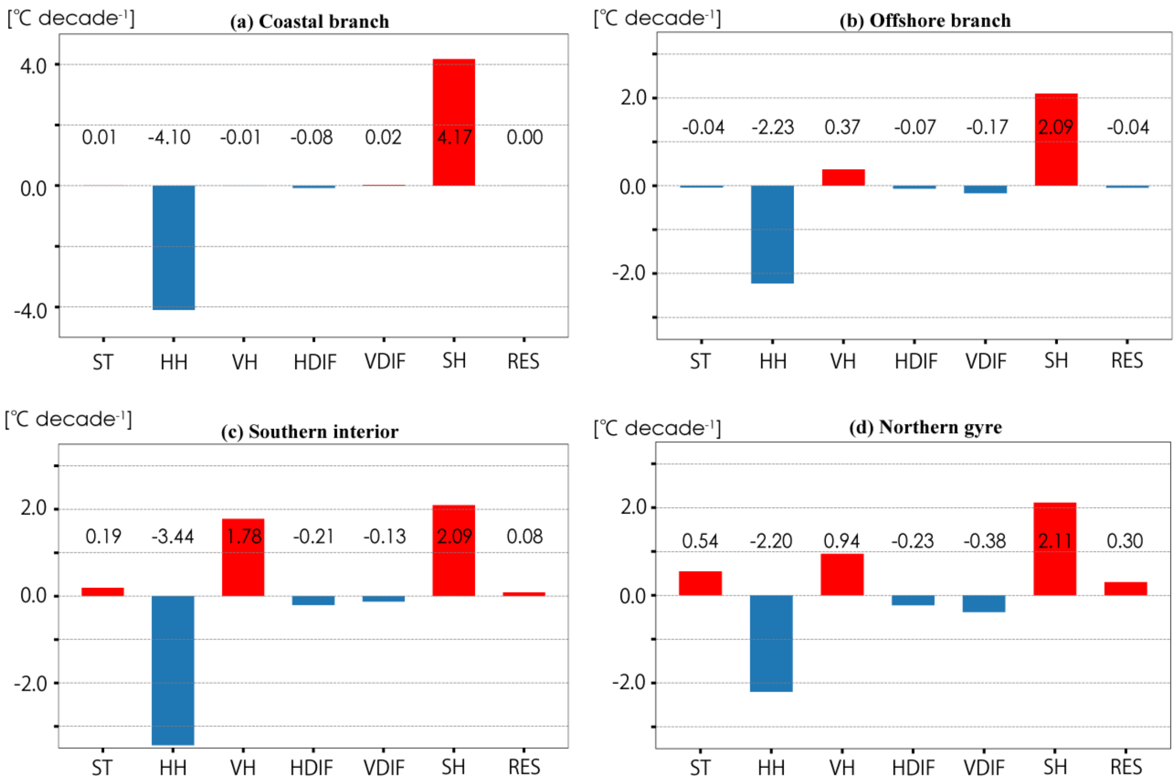

Figure 2-8. Spatial averages of ST, HH, VH, HDIF, VDIF, and SH from Eq. 2-5 are presented for the following regions: (a) coastal branch, (b) offshore branch, (c) southern interior, and (d) northern gyre. The RHS represents the residual. Red (blue) bars represent warming (cooling). Figure 8 of Matsuura and Kida (2024).

2.4.4 Sensitivity to the trend in flow field and wind stress

The flow field trend in R-WARM may also impact the SST. The most significant changes are simulated near the separation point of the western boundary current (**Fig. 2-9**), where eastward flow increases to the north, indicating a northward shift in the position of the zonal jet. This shift may partially explain the enhanced SST trend observed north of the zonal jet. Additionally, a reduction in the flow speed of the zonal jet is evident in the eastern half of the Japan Sea. However, the overall effect of these changes seems moderate, as most flow adjustments align with the SST trend contours.

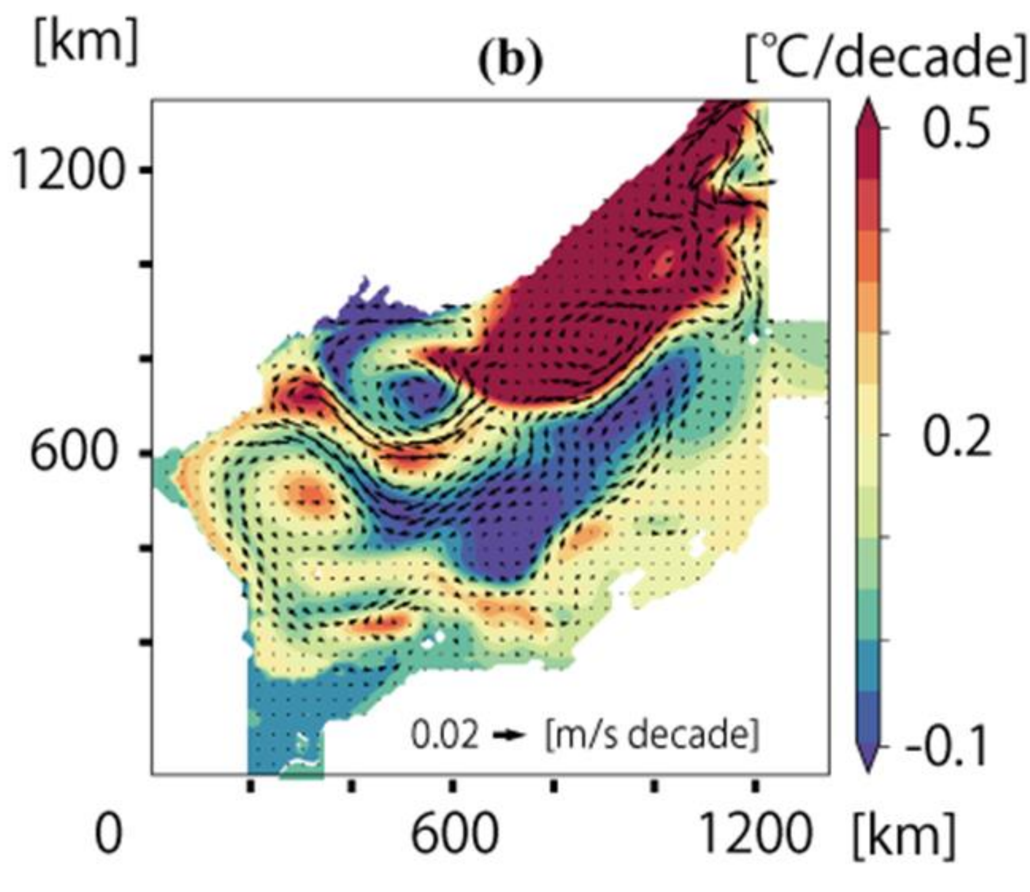

Figure 2-9. Trends in the flow field for the R-WARM experiments. Black arrows show the magnitude and the direction of the trends, and the color contours show SST trends. Figure 9 of Matsuura and Kida (2024)

To assess the model's sensitivity to the location of the separation point, we ran a model experiment where the axis of the zero wind-stress curl is shifted southward to y = 400 km. Consequently, a southward shift in the separation point occurs. The overshoot becomes weak compared to R-WARM, bringing it closer to observations (**Fig. 2-10**). A recirculation gyre develops southeast of the separation point, with a stronger SST trend than the surrounding areas, though weaker than R-WARM. The detachment mechanism at the separation point of the wind system likely affects the formation of a strong warming patch observed north of the Korean peninsula near 38 °N (**Fig. 1-1a**). We also find that the development of the zonal band structure of the SST trend is robust and not affected by the details of the wind profile.

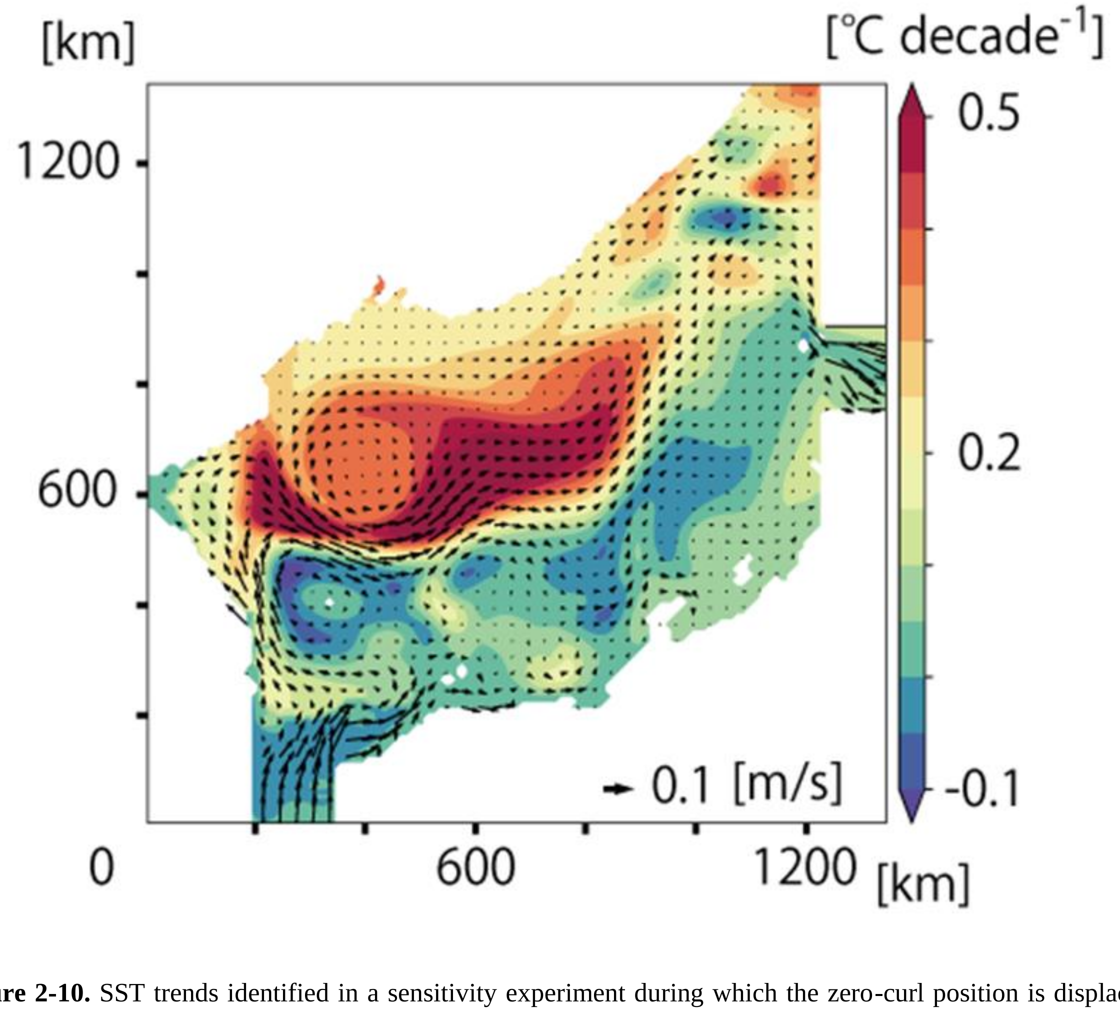

Figure 2-10. SST trends identified in a sensitivity experiment during which the zero-curl position is displaced southward (y = 400 km). The color contours show the SST trends and the black arrows show the mean currents. Figure S2 of Matsuura and Kida (2024)

2.4.5 Residence Time

Heat budget analysis examined the SST trend from an Eulerian perspective. We now estimate residence times to analyze the trend from a Lagrangian perspective.

2.4.5.1 Residence time of water masses in the coastal and offshore branches

Particles released from the Tsushima Strait split into two paths, along the northern coast of Japan and the eastern coast of Korea. They merge within a year and exit through the Tsugaru Strait (**Fig. 2-11**). Particles moving along the coast of Japan take about 130 days to reach the Noto Peninsula. It requires another 120 days to reach the Tsugaru Strait. However, some particles leave the coast and move westward with eddies. These eddies may reflect the planetary baroclinic Rossby waves, and within 100 days, they will eventually join the western boundary current. Particles moving along the coast of Korea take about 70 days to reach the offshore branch region. The particles then take about 100 days to travel eastward along the zonal jet to reach the Tsugaru Strait. Some particles disperse and exit the pathways of the throughflow to enter the southern interior or the northern gyre.

The number of particles that remain within the coastal branch is about 14 days at a depth of 50 m and 13 days at a depth of 90 m. There is little difference in residence time between these depths. This short timescale implies that the advection of cooler water from the strait directly influences the weak SST trend in the coastal branch.

The number of particles that remain within the offshore branch is longer than that of the coastal branch. It is 137 days at a depth of 50 m and 141 days at a depth of 90 m. It takes more time than the coastal branch because the particles travel a much greater distance and take time to reach the offshore branch. The residence time is estimated based on the profile after the particle numbers peak, and it is approximately 150 days after their release in the Tsushima Strait. These residence times are 137 and 141 days, shorter than a year. The short residence times are consistent with the weak SST trend expected in areas with little heat accumulation.

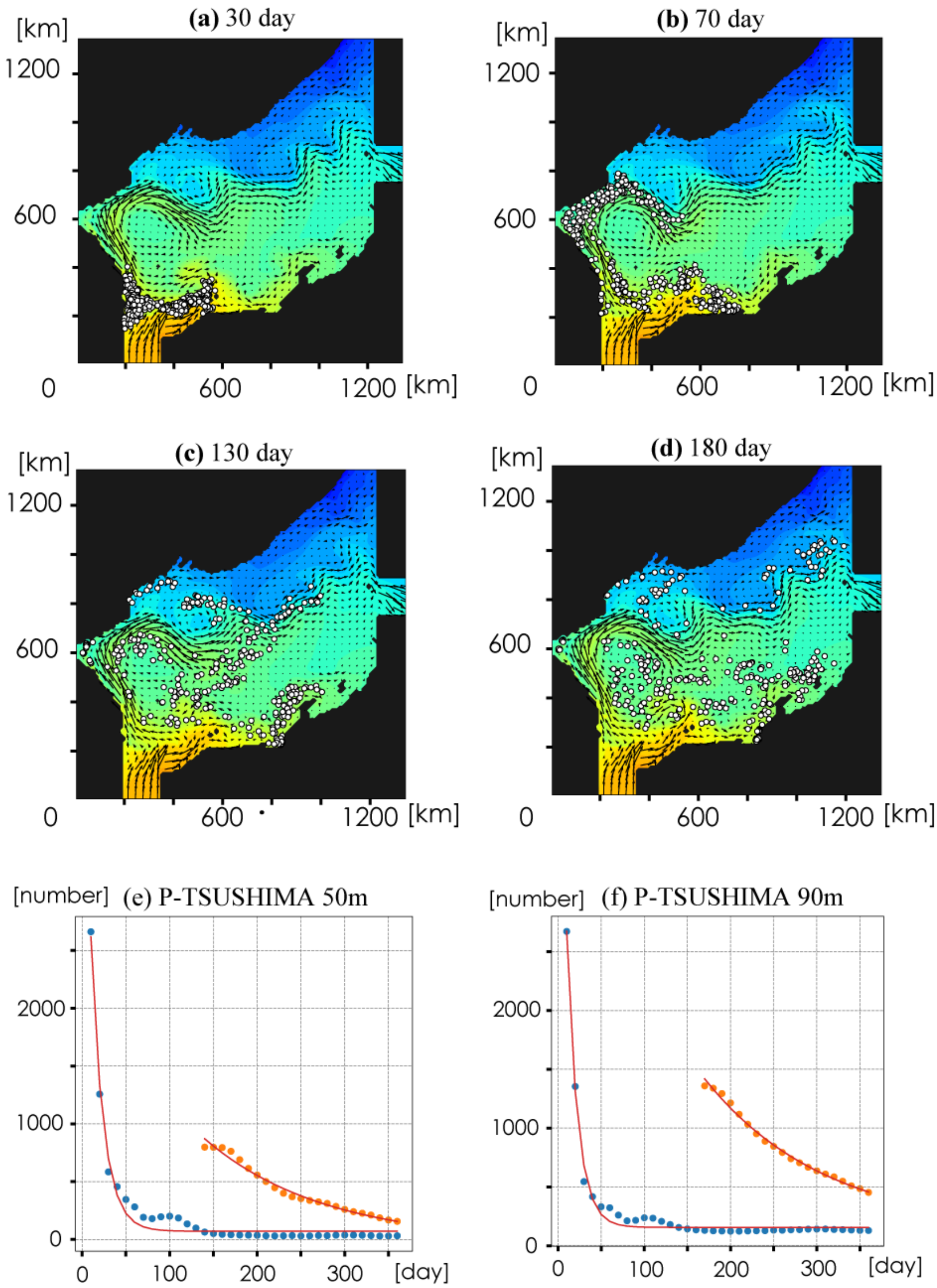

Figure 2-11. Snapshots of particles released at a depth of 50 m near the Tsushima Strait on day 0, shown at (a) 30, (b) 70, (c) 130, and (d) 180 days. Particles are displayed as white dots, with annual climatological SSTs represented by color shading and flow fields shown as vectors. Time series representing the number of particles at depths of (e) 50 m and (f) 90 m in the coastal and offshore branches are shown by blue and orange dots, respectively. The red solid line represents the best-fit exponential curve. Figure 9 of Matsuura and Kida (2024).

2.4.5.2 Residence times of water masses in the southern interior and northern gyre

P-AIR demonstrates the spatial variability of residence times inside the model domain (**Fig. 2-12a**). Around 55% of the particles are found to remain within the domain. The rest of the particles exit through the Tsugaru Strait. Residence times are long for those observed inside the recirculation gyre near the western boundary. Areas west and northeast of the Noto Peninsula and the northern gyre also have residence times that are significantly longer than those of the coastal and offshore branches (**Fig. 2-12a**). The residence times in the coastal branch, offshore branch, and southern interior are 0.08 years (29 days), 0.72 years (259 days), and 1.32 years, respectively, when spatially averaged. These residence times correspond well with the spatial pattern in the SST trend (**Fig. 2-7b**) and show strong SST trends in the southern interior, where residence times exceed one year. The residence times simulated in P-AIR align with the results from P-TSUSHIMA, indicating that residence times along the coastal and offshore branches are less than one year.

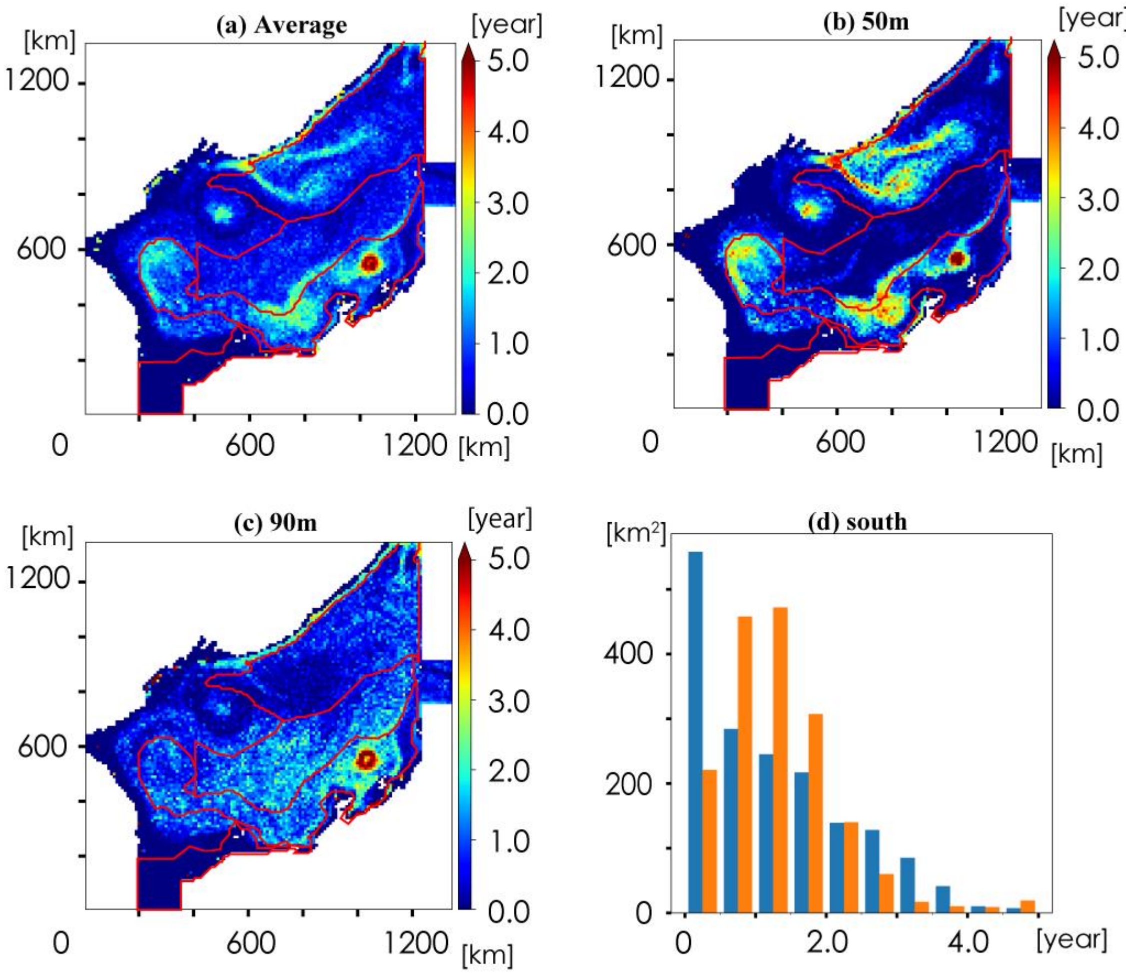

Figure 2-12. Residence times of particles in the simulation of P-AIR averaged over 100 km² following their release at (a) depths of 50 m and 90 m, (b) 50 m only, and (c) 90 m only. (d) The distribution of particle age in the southern interior region. The vertical axis shows the total area associated with each residence time. Blue and orange bars represent residence times at 50 m and 90 m depths, respectively. Figure 10 of Matsuura and Kida (2024).

Spatially averaged residence times are generally longer at a depth of 90 m compared to 50 m (**Fig. 2-12b, 2-12c**). For the coastal branch, the average residence time is 18 days at 50 m and 36 days at 90 m, which is shorter than the offshore branch. For the offshore branch, it extends to 115 days at 50 m and 407 days at 90 m. This increase in residence time is reasonable, as flow speeds are slower at greater depths. Interestingly, in the southern interior region, the residence times are nearly equal, with 468 days at 50 m and 486 days at 90 m. Particles placed at 50 m typically leave the region. However, some particles remain in the model due to eddy activity, leading to an age distribution that shows a gradual trend of exponential decay over time (**Fig. 2-12d**). Particles placed at 90 m, however, recirculate and reenter the region after about one year. This results in particle numbers that peak around 2.5 years with a rapid decay. In terms of spatial variability, surface eddies explain the increase in residence time towards the west. It is more diffused and thus uniformly distributed for deeper particles. For the intensification towards the west to establish, we find surface eddy activity to play a key role in increasing the residence time and inducing warmer SST in the southern interior zonal band (**Fig. 2-12b**).

When comparing the residence times and heat transport convergence terms from Eq. 2-5, a stronger impact of the Japan Sea Throughflow is found in areas with shorter residence times (**Fig. 2-13**). The dispersion of particles for P-AIR shows that the number of particles decreasing rapidly in time is where the heat transport convergence term is strongly negative, corresponding to areas with short residence times (**Fig. 2-12**). These regions exhibit weak SST trends. In the southern interior and northern gyre, however, many particles converge where the negative impact of heat transport convergence is less significant, and some areas even show positive values. These regions have longer residence times and exhibit strong SST trends.

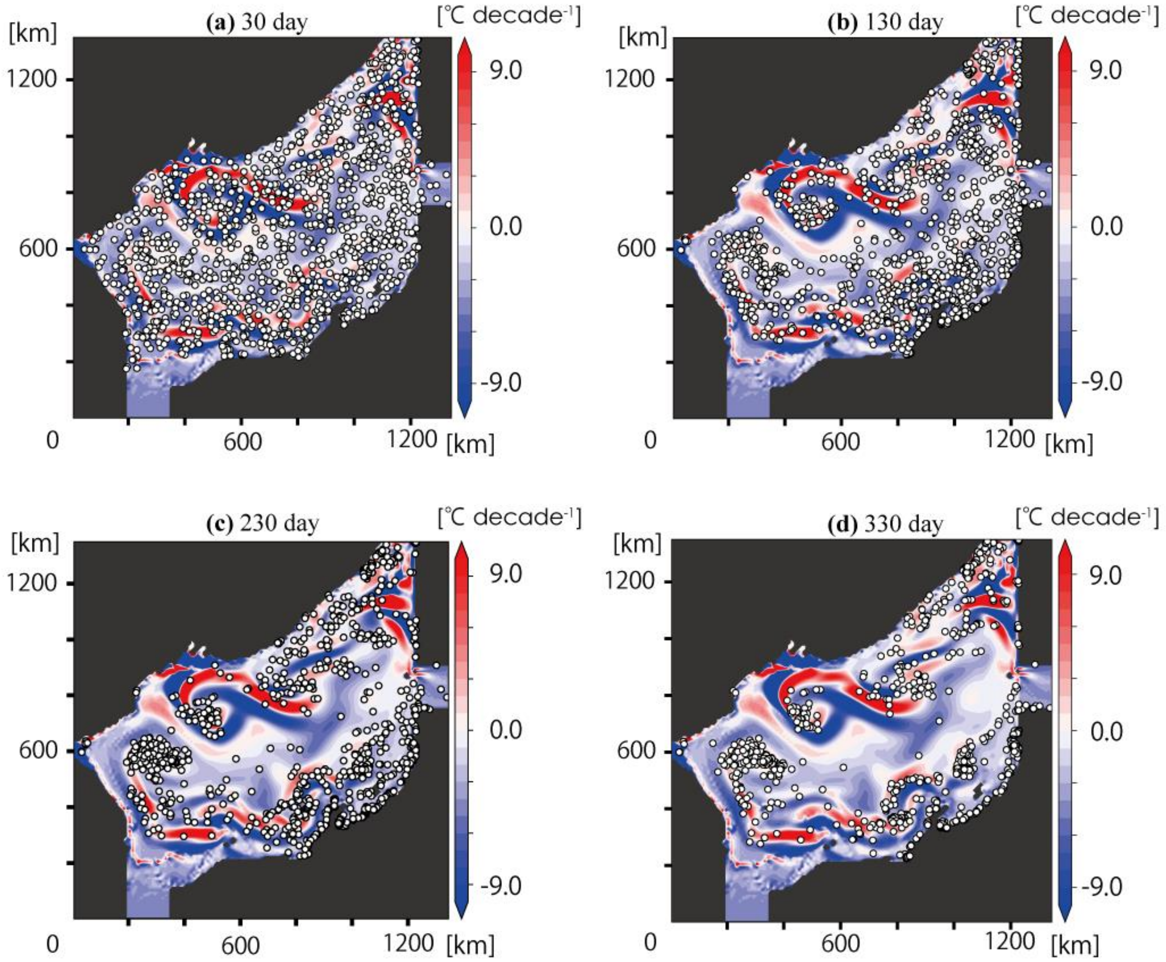

Figure 2-13. The numbers of P-AIR particles at a depth of 50m at (a) 30, (b) 130, (c) 230, and (d) 330 days. White dots: Particles. The background color shows the sums of the horizontal and vertical heat transport convergence terms. Figure 11 of Matsuura and Kida (2024).

2.5 Conclusion

Satellite observations show a trend of SST warming with a meridional alternating zonal band pattern. The mechanism behind this observed spatial pattern was investigated in this chapter, based on a hypothesis that the spatial pattern reflects varying residence times within the Japan Sea due to the Japan Sea Throughflow. Heat accumulation is prevented along the throughflow path, introducing water with a weak SST warming trend, leading to less pronounced SST warming than interior regions.

Using an idealized rectangular coastline model, we successfully simulated a meridionally alternating zonal band structure even under spatially uniform atmospheric warming at the surface. This model consisted of a flat bottom and two straits with a flow analogous to the Japan Sea throughflow. An inflow occurs at the southwest corner, which will bifurcate with one branch flowing along the southern and eastern coastline to exit the outflow strait, which exits in the middle of the eastern boundary. Another branch flows along the western boundary before becoming a zonal jet flowing offshore at the latitude of the outflow strait. The zonal band emerges because the throughflow bifurcates within the Japan Sea, and the interior warms faster than it does along the pathway of the throughflow. Thus, zonal bands of weak SST warming form along the two bifurcating flows, and between these two flows, strong SST warming occurs. A meridionally alternating zonal band structure is then established.

When realistic coastline and bathymetry exist, model experiments still show a meridionally alternating zonal band structure similar to the idealized model. The experiment further suggests that a stable recirculation gyre enables a region with a patch of strong warming to form along with a stronger trend towards the west. Additionally, a steep shelf diffuses the flow east of the Noto Peninsula and enables a zonal band with a strong SST trend to form, which matches well with observations. Heat budget analysis shows the importance of the Japan Sea Throughflow in mitigating the SST increase. It indicates that the coastal and offshore branches are where weak SST trends form because the cooling effect induced by horizontal heat transport convergence diminishes the warming effect induced by surface heat flux.

Differences in residence time coincide with the strong and weak SST warming trends from particle release experiments. The residence times along the path of the Japan Sea Throughflow are short, about 15–150 days. Therefore, the impact of warming by surface heat flux on water parcels along the path is limited. In contrast, residence times in the southern interior region are much longer, ranging from 1 to 3 years. Inside eddies is where the longest residence times are found. As a result, a patch of strong warming region forms near the western boundary of the study domain.

To examine the basic mechanism behind the SST warming of the Japan Sea, our model experiments focused on the role of external forcings in driving the spatial variability of the SST warming trend and simplified various processes. Variability in internal processes can also play a role. In Chapter 4, we will discuss the impact of variability in the subpolar front, one of the prominent features of the Japan Sea, which may impact our results.

Chapter 3 SST response to changes in the location of the SST front

3.1 Introduction

The meridional position of the subpolar front in the Japan Sea may be crucial for understanding the spatial variability of the SST warming trend since the subpolar front is where the strongest meridional SST gradient exists (Kida et al., 2015). The front's position exhibits notable year-to-year and decadal variability (Park et al., 2004; Choi et al., 2009; Chen et al., 2022). Recently, Chen et al. (2022) examined the long-term positional changes of the SST front, discovering a gradual southward shift in the central Japan Sea (130-135°E) and a northward shift in the eastern Japan Sea (135-138°E). However, the link between the long-term shifts of the SST front position and that of the jet, often corresponding to where the maximum subsurface horizontal temperature gradient exists, remains poorly understood. Choi et al. (2009) utilized satellite altimeter data from 1993 to 2001 to examine the jet position and revealed significant north-south oscillations.

How will a meridional shift of the SST front affect the SST warming trend? If the front shifts sinusoidally with a northward shift in the east and a southward shift in the west, a maximum patch will form in the east, and a minimum patch will form in the west (**Fig. 3-1**). This chapter aims to investigate the impact of such SST frontal shift to the SST trend from 1993 to 2019 and how it is related to the change in jet position, a critical component of the oceanic circulation of the Japan Sea. We focus on how they may be behind the formation of maximum and minimum patches in the SST trend within the zonal band structure. Section 3.2 describes the satellite data and methods used to detect the SST front and the latitudinal location of the jet. Section 3.3 presents the results. Finally, Section 3.4 provides conclusions and discussion in this chapter.

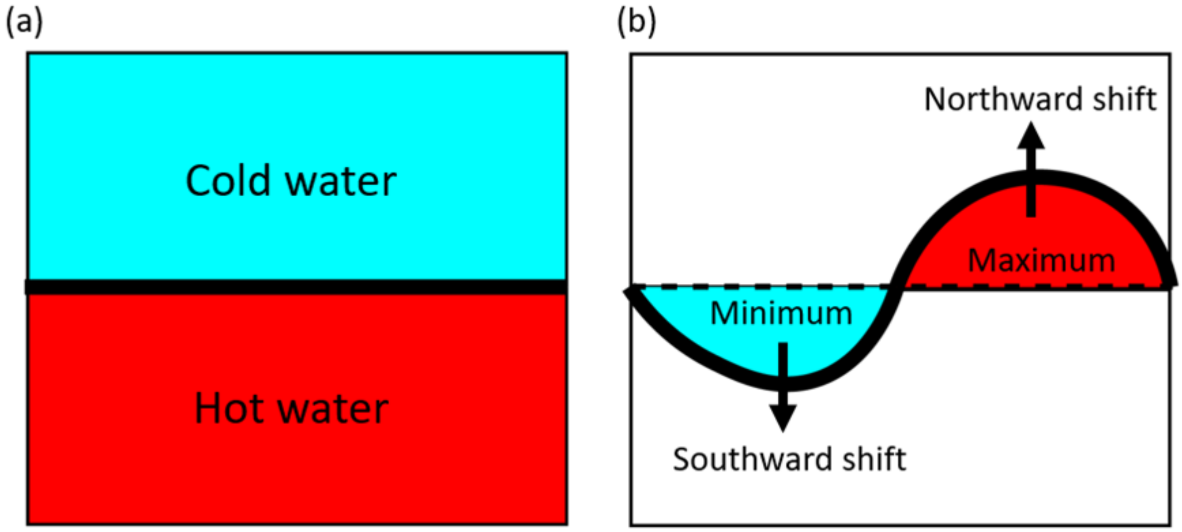

Figure 3-1. Schematic diagrams of the SST and thermal front. The color and thick black line represent temperature and thermal front. (a) The mean state of the SST and thermal front position. (b) A snapshot of the gradual shift of the thermal front and the possible response due to the front shift.

3.2 Method

3.2.1 Data

We use satellite-based datasets to detect the SST front and jet positions. Optimum Interpolation SST dataset V2 distributed by the National Oceanic and Atmospheric Administration (NOAA) is used for SST. For velocity, absolute dynamic topography (ADT), Ocean Gridded L4 Sea Surface Heights and Derived Variables Reprocessed distributed by the Copernicus Marine Environment Monitoring Service (CMEMS) are used. Both datasets have the same spatial resolution (0.25°×0.25°) and time resolution (daily). In this study, we used the daily dataset for 27 years, from 1993 to 2019, to match the ADT dataset that started in 1993. We downloaded the SST dataset in March 2021 from (https://apdrc.soest.hawaii.edu/index.php) and the ADT dataset in June 2021 from (https://data.marine.copernicus.eu/products?option=com_csw&amp%3Btask=results) from 127°E to 143°E and from 34°N to 50°N.

3.2.2 Detecting the position of the SST front and jet

3.2.2.1 Position of the SST front

To detect the position of the SST front in the Japan Sea, we first calculate the SST gradient from the daily SST dataset:

$$SST gradient(t,x,y) = \sqrt{\left(\frac{\partial T}{\partial x}\right)^2 + \left(\frac{\partial T}{\partial y}\right)^2} \qquad (3-1)$$

where t is daily time, x is zonal distance and y is meridional distance. We then find the latitude of the maximum SST gradient for each longitude starting from west to east and define it as the location of the SST front (**Fig. 3-2a**). We will examine within 37°N to 42°N where the SST front is often found. This procedure is repeated every day from 1993 to 2019. We will then estimate the long-term shift in the location of the SST front and the strength of the SST gradient along this front.

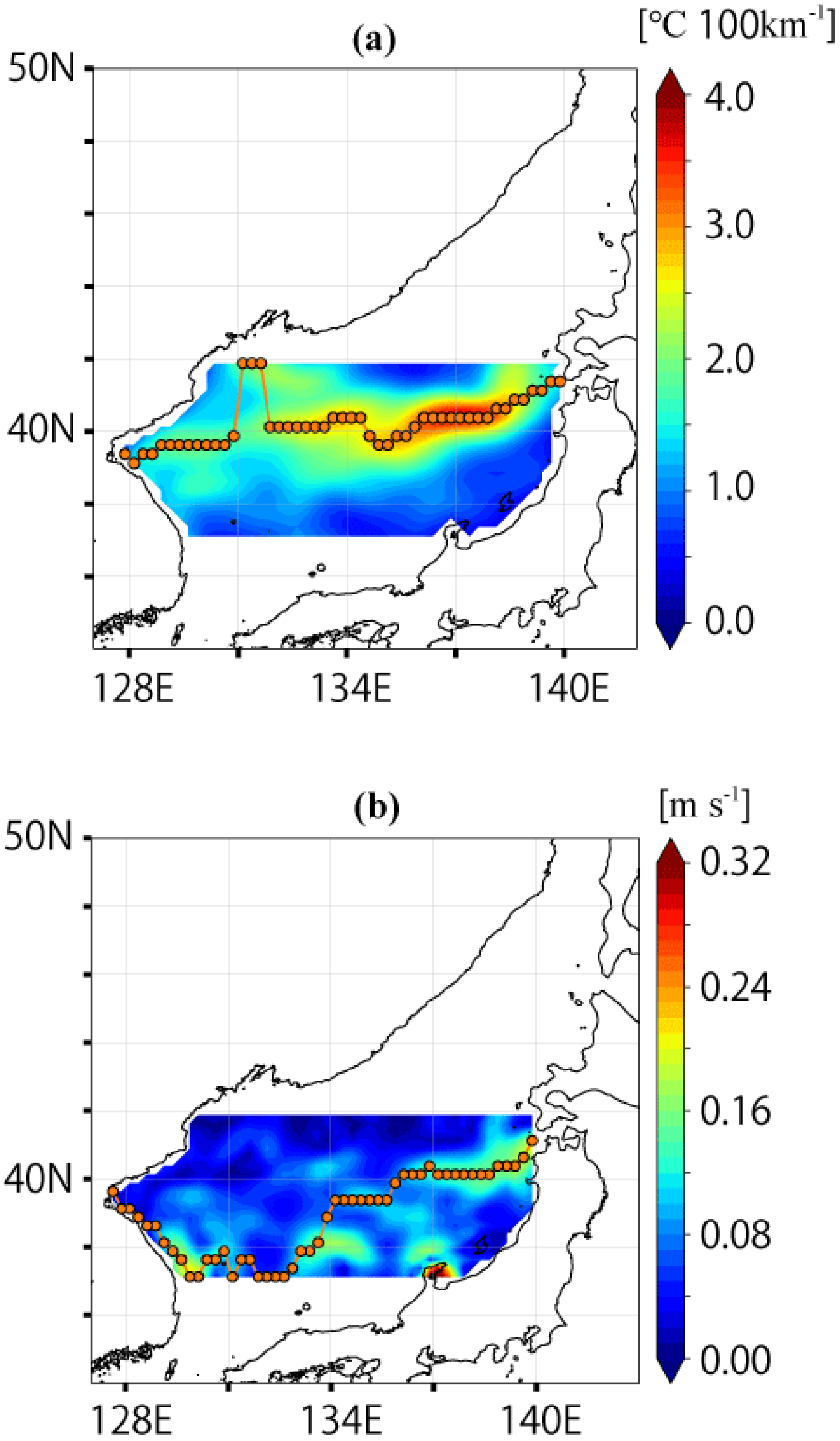

Figure 3-2. (a) SST front and (b) jet based on the annual mean SST and ADT. The color shows the magnitude of the SST gradient and current speed. The orange dots show the maximum SST gradients or current speeds at each longitude.

3.2.2.2 Position of the Jet

To detect the jet position, we first calculate the geostrophic current from daily ADT:

$$u = -\frac{g}{f}\frac{\partial ADT}{\partial y}, v = \frac{g}{f}\frac{\partial ADT}{\partial x} \qquad (3-2)$$

where *u* is zonal surface geostrophic current, *v* is meridional surface geostrophic current, *g* is the gravitational constant (9.8 m^2 s^{-1}), and *f* is the Coriolis parameter. We then calculate the current speed:

$$current\ speed(t,x,y) = \sqrt{\left(\frac{\partial u}{\partial x}\right)^2 + \left(\frac{\partial v}{\partial y}\right)^2} \qquad (3-3)$$

Since the paths of the currents in the Japan Sea are complicated (Kawabe et al., 1982a; Yabe et al., 2021), we employ three-step detecting procedures to find a continuous jet path across the Japan Sea. First, we examine the latitudinal variance of the maximum current speed in each longitude. The position of the jet is assumed to be similar to the location of the maximum current speed. Second, we search the location of the jet by searching the location of maximum current speed starting from east to west rather than from west to east, like the approach used for detecting the SST front. Starting from the east ensures that the jet exits through the Tsugaru Strait. Third, we will select the maximum position of the current speed within 1 standard deviation of the latitudinal variance of the jet that was estimated in the first step. This last third step ensures that the path of the jet is continuous and does not abruptly switch to the paths of different currents.

3.2.3 Estimating SST Response due to a shift of SST front

To evaluate the SST response induced by the shift of the SST front, we estimate the magnitude of the SST warming trend based on the meridional gradient of the SST and changes in the latitudinal location of the jet (L_{SPF}):

$$\frac{\partial T}{\partial t} = \frac{\partial T}{\partial y}\frac{\partial L_{SPF}}{\partial t} \qquad (3-4)$$

The left side is the tendency term. The right-side term is the meridional gradient of the SST and the long-term shift in L_{SPF}. By partitioning each parameter of Eq. 3-4 (A) into steady ($\bar{A}$) and trend ($A^{'}$) components, we can an equation that can estimate the SST response due to the shift in the position of the SST front:

$$\frac{\partial T^{'}}{\partial t} = \frac{\partial \bar{T}}{\partial y}\frac{\partial L_{SPF}{}^{'}}{\partial t} + \frac{\partial T^{'}}{\partial y}\frac{\partial \bar{L}_{SPF}}{\partial t} \qquad (3-5)$$

We have neglected the second-order terms. The second term in the RHS of Eq. 3-5 is zero because $\frac{\partial \bar{L}_{SPF}}{\partial t} = 0$. The terms in Eq. 3-5 show the SST responses induced by the shift in L_{SPF} in the presence of a meridional SST gradient:

$$SST\ response = \frac{\partial \bar{T}}{\partial y}\frac{\partial L_{SPF}{}^{'}}{\partial t} \qquad (3-6)$$

The long-term average of the meridional SST gradients can be estimated from the climatological SST. The shift in the latitudinal location of the L_{SPF} can be estimated using a least square method.

3.3 Results

3.3.1 Overviews of annual mean SST gradient and ocean current

For the annual mean SST, strong SST gradients are found in the middle of the Japan Sea with a maximum on the eastern side of the sea from 136 to 138°E (**Fig. 3-3a**). The magnitude is greater than 3.5 °C 100 km^{-1} and extends in a zonal direction between the warm (cool) water occupying the south (north) of the Japan Sea (**Fig. 1-1a**). The SST front bifurcates from 132°E to 133°E on the western side of the Japan Sea. Park et al. (2004, 2007**)** suggest that this feature is linked to the strong northwesterly wind blowing in winter. The weak and moderate SST trend patches found within the zonal band structure around 40°N are likely to be connected to the meridional shift in the SST front.

For the annual mean flow field, a strong zonal flow appears around 40°N where the significant SST front exists, and the current speed is more than 0.1 m s^{-1} (**Fig. 3-3 b c**). Strong meridional currents are found along the Korean and Japanese coasts, known as a branching system in the Japan Sea (Kawabe 1982a; Yabe et al., 2021). However, these meridional currents are not directly linked to the strong SST gradient position. The location of strong zonal current syncs with the strong SST gradients found on the western and center parts of the Japan Sea (**Fig. 3-3c**), confirming that the position of the zonal jet is linked to the position of the SST front. We find a current flowing out through the Tsugaru Strait and another current flowing along the western coast of Hokkaido that eventually exits to the Soya Strait. This northward current advects warm water to the northern part of the Japan Sea and may be behind the formation of a moderate SST front found at 44 °N. This chapter focuses on the most significant SST front and its connection to the jet in the middle of the Japan Sea.

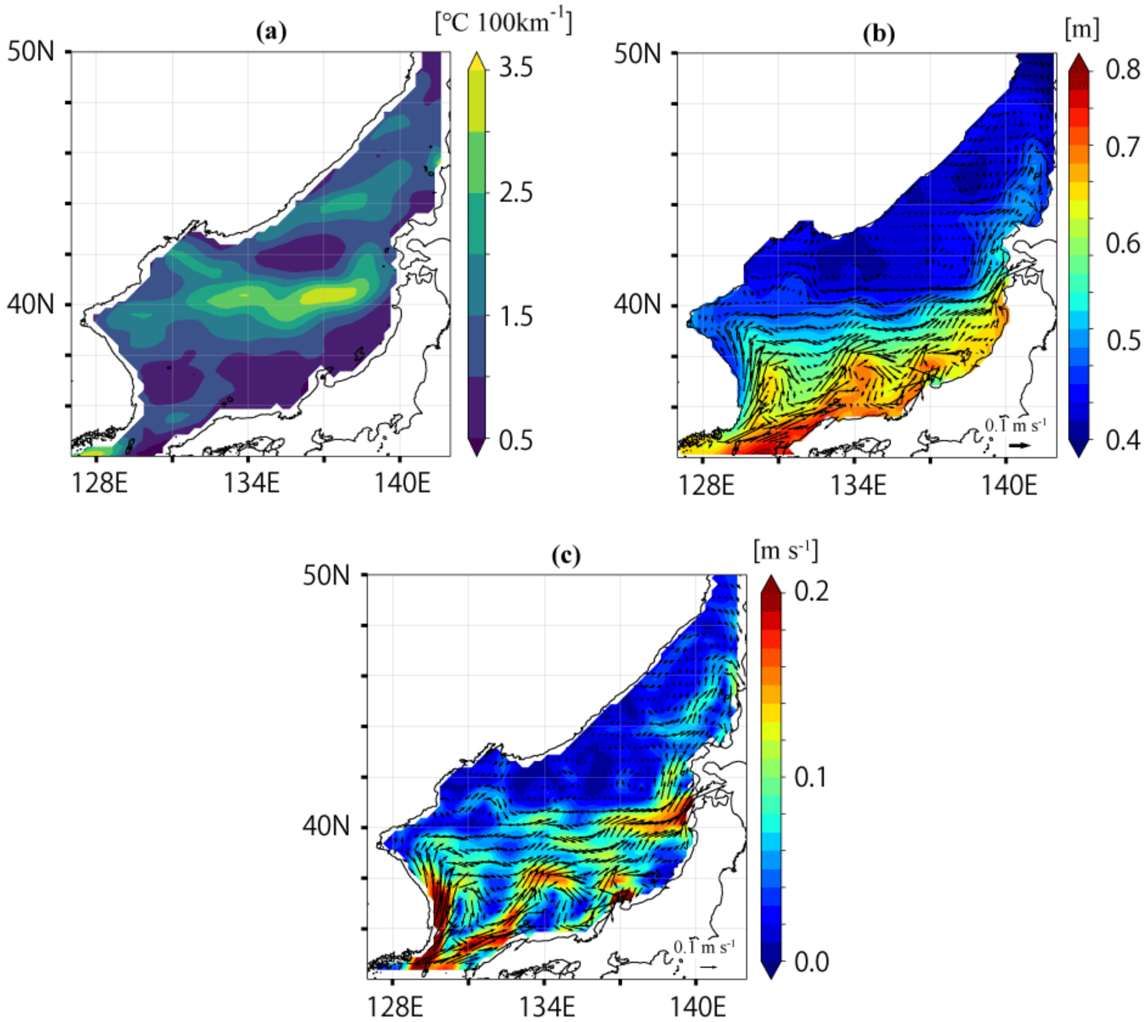

Figure 3-3. (a) The magnitude of the annual SST gradient. (b) The annual absolute dynamic topography. (c) The geostrophic current speed. The arrows show the direction of the geostrophic current.

3.3.2 Mean Positions of SST front and jet

The mean position of the SST front, as evaluated from daily SST, appears to be around 40°N (**Fig. 3-4a**). This position agrees with what was found in the annual mean and the location of the zonal band structure of the weak SST trend discussed in the previous chapter. Interestingly, the SST front position does not completely coincide with the center of the maximum and minimum patches and is dislocated either south or north. However, the distance is within 1 σ and suggests that the generation of these patches may be connected to the changes in the SST front. The standard deviation of the SST front position varies with each longitude but is generally broader in the west (120 ~ 130 km) than in the east (70 ~ 80 km). This is because the seasonal variation in the SST front position is bigger on the western side due to the strong winter monsoon from the continent, which agrees well with the results of Park et al. (2004, 2007). The magnitude of the meridional SST gradient along the SST front remains almost the same (4.5 ℃ 100 km^{-1}) from the west to the east of the Japan Sea but with a slight increase to the east where the minimum patch exists. The meridional SST gradient decreases significantly near the Korean coast and Tsugaru strait (**Fig 3-4c**).

The mean position of the jet evaluated from the daily SSH gradient exists south of the SST front (**Fig 3-4b**). The distance between the SST front and jet becomes wider (150 km) in the west (131°E~134°E) than in the east. Near the Tsugaru Strait, it is only 30 km apart, suggesting that the location of the two fronts is more strongly connected on the eastern side than on the western side. The mean position of the jet on the western side is located in the center of the maximum patches of the SST trend likely because many mesoscale eddies are reported in this region (Isoda 1994b; Yabe et al., 2021), and the mean jet position changes depending on the strength of eddies.

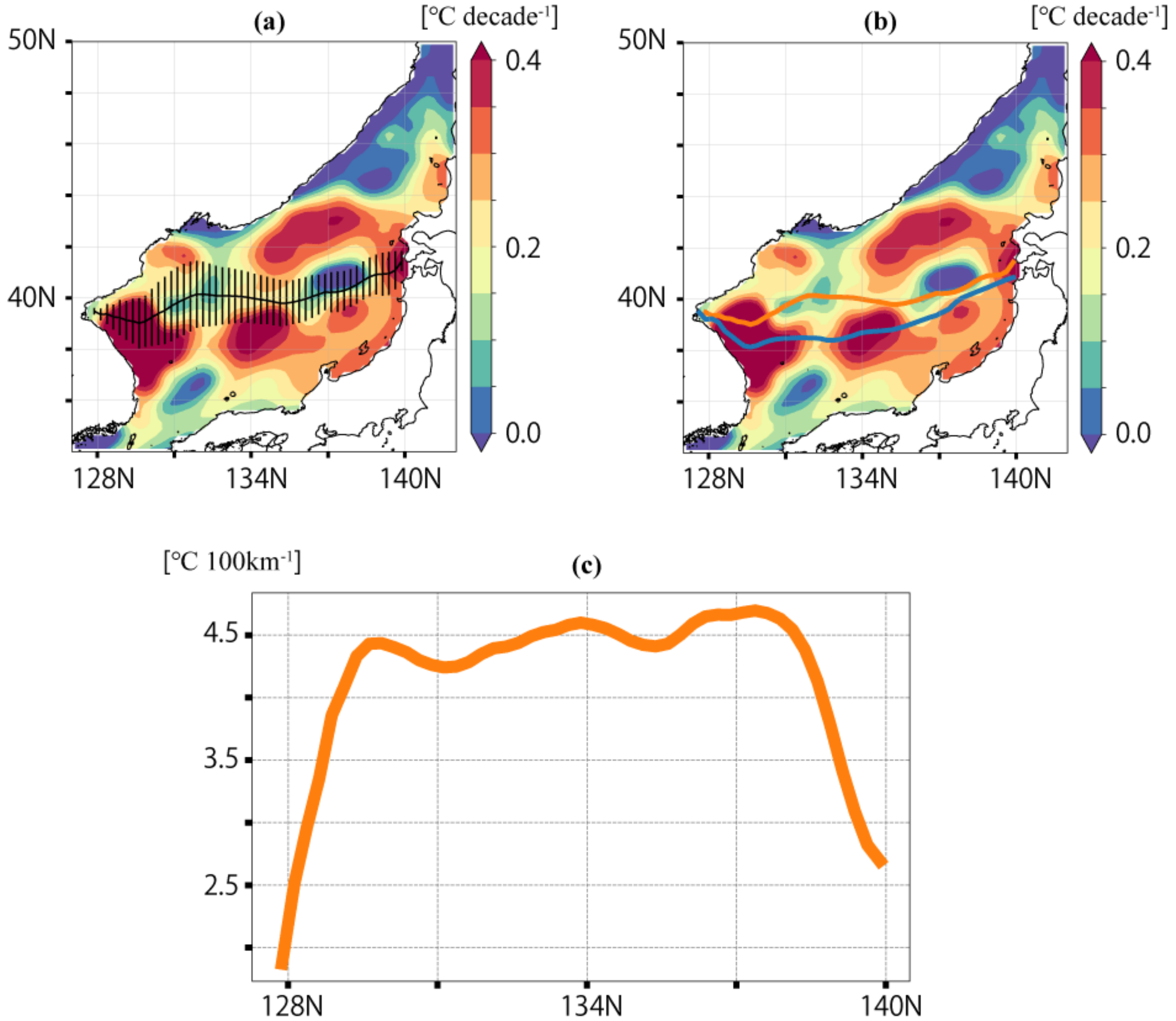

Figure 3-4. (a) The mean position of the SST front. (b) The mean position of the jet (blue) and SST front (orange). (c) The magnitude of the SST meridional gradient. The background color shows the SST trend and the black bars in (a) show the variance of the SST front from 1993 to 2019.

3.3.3 Changes in the SST frontal position between the former and latter periods

The SST front exhibits complicated meridional movement from the west to the east. Figure 3-5 ab shows the location of the SST front found every 0.25 degrees in latitude in terms of frequency for 1993-2002 and 2010-2019. A sharp single peak will correspond to a case where the front does not move much and remains in one place. A value of 0.5 will mean that the front is found at that location for 50% of the time. The frequency distribution of the SST frontal position shows changes in the behavior of the front from 1993-2002 to 2019-2019, such as the strengthening and weakening of existing peaks, the emergence of a new peak, and the stabilization of the front. Based on these characteristics, we roughly divide the area into three zones (Zones 1, 2, and 3) to examine the differences in the frontal location. We shall call the first 10 years (1993-2002) and the last 10 years (2010-2019) the former and the latter periods, respectively.

(a) Zone 1 [129.125°E~ 129.825°E]

The distributions of the SST frontal position for both the former and latter periods are widely spread with values around 0.1 from 38°N to 41.5°N. There are two distinct peaks, around 38.5°N and 40°N (**Fig. 3-5 c**). Compared to the first period, the latter period shows the distribution to increase around 40°N and decrease around 38.5°N. This feature suggests strengthening the northern front compared to the southern front, thus a northward shift of the SST front from 1993 to 2019.

(b) Zone 2 [133.125°E ~ 134.875°E]

The distribution of the SST frontal position in the former period shows the peak around 40°N to be slightly north than that found in Zone 1 (**Fig. 3-5d**). This peak spreads from 39°N to 41°N with a magnitude of 0.1 and corresponds to the annual mean position of the SST front (**Fig. 3-3a**). In the latter period, we find an emergence of a new peak at 39.5°N, thus a southern shift in frontal position. This new peak emerges primarily for Zone 2 and is not a result of a gradual southern shift of the front that existed just north of 40°N. This feature implies that the north-south position of the SST front fluctuates significantly in this area.

(c) Zone 3 [135.125°E ~ 138.125°E]

The distribution of the SST frontal position shows a single peak around 40.5°N for both former and latter periods that resembles a Gaussian distribution (**Fig. 3-5 e**) with a maximum of 0.28 in the former period. This value increases to 0.33 in the latter period and is associated with a slight decrease in the north and an increase in the south (from 39°N to 40.5°N). This gradual shift is found from 136°E to 138°E (see Appendix), and the SST front gradually shifts southward in this area.

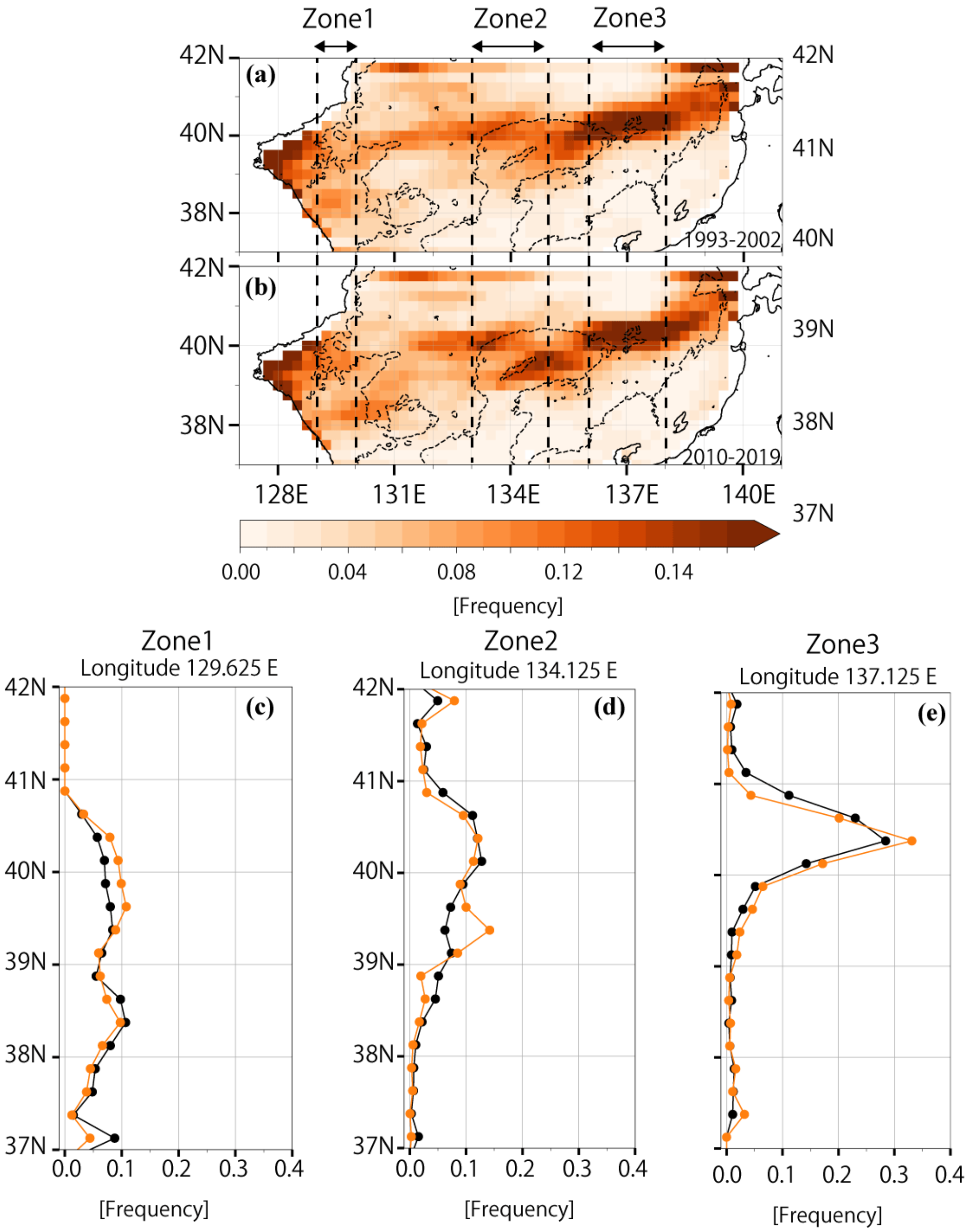

Figure 3-5. The frequency distribution of SST front position from (a) 1993-2002 and (b) 2010-2019. (c) The meridional cross-section of the frequency distribution at (c) 129.625°E, (d) 134.125°E, and (e) 137.135°E. The black (orange) dot and line show the frequency from 1993-2002 (2010-2019) at the shown longitude. The dashed black contour in the a and b shows the depth at -2000m.

3.3.4 Changes in the jet position between the former and latter periods

The frequency distribution of the jet position exhibits a complicated meridional movement from the west to the east, more than that for the SST front. A new peak emerges in many regions except close to the Tsugaru Strait (138°E ~ 140°E) (**Fig. 3-6 a, b**). An interesting aspect of these new peaks is that they emerge about 100 km away from the original peak, suggesting the influence of mesoscale eddies. Here we will examine the changes in the jet position and its connection to the SST front based on the three zones used to examine the SST front. As before, we will call the first 10 years (1993-2002) the former period and the last 10 years (2010-2019) the latter period.

(a) Zone1 [129.125°E~ 129.825°E]

The distribution of the jet position exhibits an exponential decay from the south to the north (from 37°N to 41°N) for both former and latter periods (**Fig. 3-6 c**). This distribution implies that the jet detaches from the Korean coast between these latitudes with a frequency of only 0.05 around 40°N. When examined more closely, we find an increase in the frequency at 39.5°N for the latter period, where we found the largest increase in the frequency for the SST front (**Fig. 3-5 c**). We also find the frequency of the jet around 38.5°N to slightly decrease in the latter period, where the frequency of the SST front also decreases. The characteristics of these features can be found throughout Zone 1 (see Appendix). Although these signals appear subtle and overwhelmed by the variability of the jet along the Korean coast, the analysis supports that the northern shift in the SST front and the northern shift of the jet co-occurred.

(b) Zone 2 [133.125°E ~ 134.875°E]

The distribution of the jet position exhibits a peak at 38.3°N for both former and latter periods. However, this peak is not directly connected to the SST front (**Fig. 3-5d**). The peak around 40°N likely relates to the SST front for the formal period, but this peak weakens, and another peak evolves at 39.3°N in the latter period (**Fig. 3-6 d**). A southward shift in jet position, with a distance of almost 100 km, is observed throughout Zone 2. This could capture the variability due to the formation of a mesoscale eddy in this area, which was also found for the SST front. The southward shift in the position of the jet from around 40°N to 39.3°N appears to be connected to the southward shift of the SST front (**Fig. 3-5d**).

(c) Zone 3 [135.125°E ~ 138.125°E]

The distribution of the jet position exhibits a peak around 40°N for both the former and latter periods. This latitude matches where the SST front exhibits a single peak (**Fig. 3-5e**). A new peak emerges at 39.3°N in the latter period for the jet while the frequency at 40°N decreases (**Fig. 3-6 e**). The difference between the two periods suggests that the jet position shifted southward about 100 km south. This is somewhat different from the changes in the SST front, where there was a minor southward shift, which may reflect the changes in the thermocline and eddy activity. Nonetheless, the behavior of the jet and the SST front position imply that they both moved southward.

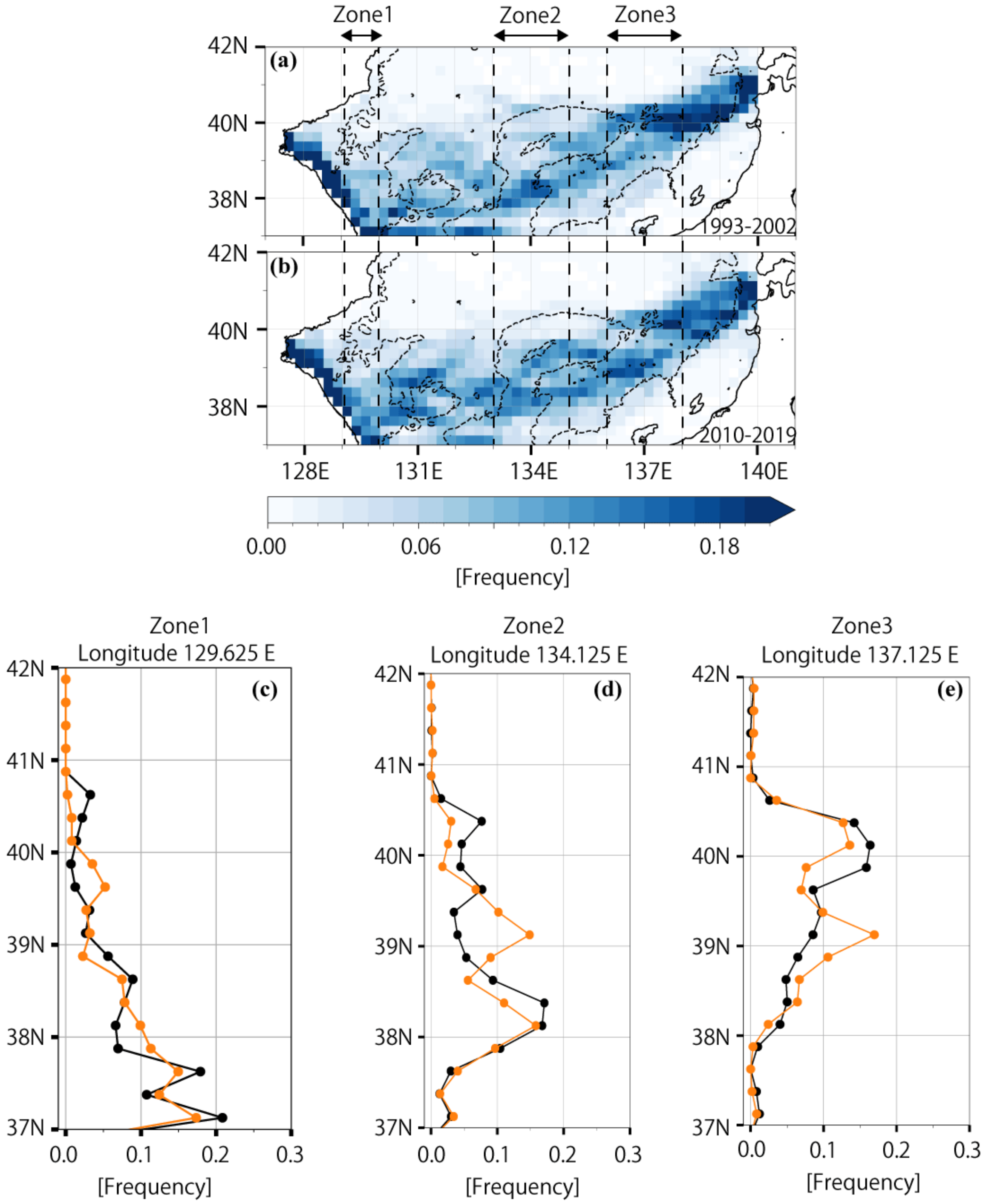

Figure 3-6. The frequency maps of jet position from (a) 1993-2010 and (b) 2010-2019. (c) The meridional cross-section of the frequency map at (c) 129.625°E, (d) 134.125°E and (e) 137.125°E. The black (orange) dot and line show the frequency from 1993-2002 (2010-2019) at the shown longitude. The dashed black contour in the map shows the depth at -2000m.

3.3.5 Shift of the SST front and jet from 1993 to 2019

Frequency distribution for the position of the SST front and the jet show different behavior for the western (zone 1), central (zone 2), and eastern (zone 3) parts of the Japan Sea (**Table 1**). Zones 2 and 3 show the SST and the jet move southward, while zone 1 shows a northward shift. Zone 2 also shows high eddy activity. The meridional movement of the SST front is not uniform zonally, thus cannot explain the zonal band structure of the SST trend, supporting the result of Chapter 2.

Table 1: The direction of the meridional movement for the SST front and the jet from the former to the latter period.

	SST front	jet
Zone 1 129.125°E ~ 129.825°E	Northward	Northward
Zone 2 133.125°E~134.875°E	Southward	Southward
Zone 3 135.125°E~138.125°E	Southward	Southward

To evaluate changes in the SST trend induced by the shift in the SST front, we will use Eq. 3-6. Estimation of the shift in the SST front and the jet based on linear fitting of their daily positions (**Fig. 3-7**) shows differences in the behavior of the SST front and the jet for the three zones, compared to that discussed in 3.3.3 and 3.3.4.

For Zone 1, the SST front shows a northward shift. The distance of this shift is 0.2 °N decade^{-1} and is larger than Zone 2 and 3. The jet also shows a northward shift, which matches the SST front, although the distance is now about half 0.1°N decade^{-1}. The direction of the shift agrees with that expected from the frequency distribution (**Fig. 3-5c, 3-6c**).

For Zone 2, the SST front shows a northward shift. The distance of this shift is 0.1°N decade^{-1}, smaller than Zone 1. On the other hand, the jet shows a southward shift, opposite to that of the SST front, with a distance of -0.05 °N decade^{-1}. The direction of the shift agrees well with that expected from the frequency distribution for the jet but not the SST front (**Fig. 3-5b, 3-6b**). The analysis implies that linear fitting may be inadequate when eddy activity is high and multiple peaks exist.

For Zone 3, the SST front shows a southward shift. The distance of this shift is 0.1°N decade^{-1}, the same as Zone 2. The jet, however, shows a northward shift, opposite to that of the SST front. The direction of the jet is different from what is found in the frequency distribution. The difference may be due to the frequency distribution having multiple peaks, as the frequency for the jet has multiple peaks like that found for zone 2.

We now compare the magnitude of the observed SST trend at the annual mean position of the SST front to that estimated based on the frontal shift using Eq. 3-6 (**Fig 3-8**). In Zone 1, both observation and estimate show a strong SST trend with magnitudes of about 0.8 ℃ decade^{-1}. The northern shift of the SST front has the potential to explain the SST trend around this area. However, the estimate for Zone 2 is not well estimated since the magnitude of the shift based on linear fitting does not represent the actual frontal shift. If we use a shift of -0.05 °N decade^{-1} estimated from the jet, Zone 2 shows cooling, which matches that observed when adding the background SST warming. Such background effect is not included in Eq. 3-6. For Zone 3, the estimated SST trend shows a cooling of -0.4 °C decade^{-1}. Considering the effect of the background SST warming, such a value is reasonable and explains the local minimum of the observed SST trend well.

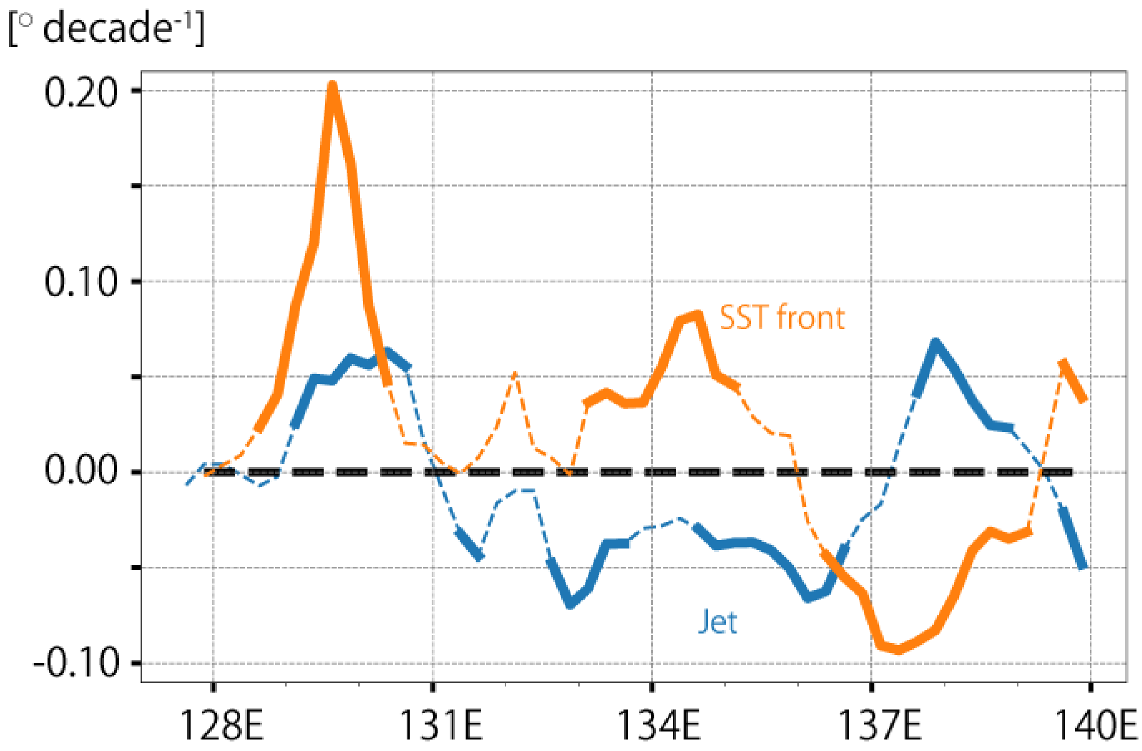

Figure 3-7. The shift distance of the SST front and jet from 1993 to 2019. The orange (blue) line represents the SST front (jet). The thick line means that the shift distance is statistically significant at the 99% confidence level using the student t-test.

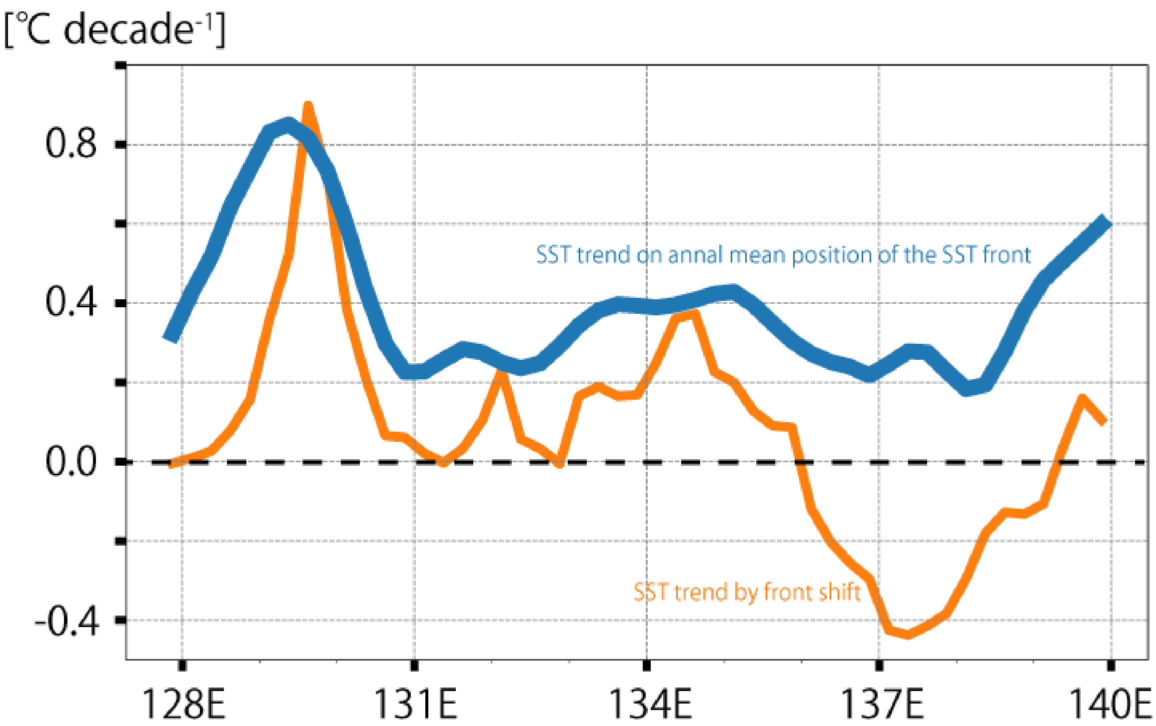

Figure 3-8. The blue line represents the SST trend along the mean SST front, and the orange line represents the SST trend due to the shift of the SST front. The effect of the SST front shift is estimated by multiplying the shift distance in Fig. 3-7 with the annual mean meridional SST gradient.

3.3.6 Changes in the surface flow field

Changes in the position of the subpolar front can successfully explain the spatial variability of the SST trend along the front. However, since the distance that the front moves is limited to about 100 km, the spatial variability of the SST trend cannot be seen elsewhere. Here, we discuss the impact of changes in the flow field. Northward current trend can play an additional role in establishing the maximum patches of the warming trend by advecting warm water from the south. The Japan Sea has a stronger temperature gradient in the meridional direction than in the zonal.

Based on the sea surface height gradient trend, an increasing trend in surface geostrophic flow is found along the Korean coast. This area corresponds to where the maximum patch of SST trend with over 0.5 ℃ decade^{-1} occurs (**Fig. 3-9a**). The meridional cross-section of the surface geostrophic flow at 37.125 °N shows an increase of about 0.02 m s^{-1} decade^{-1} along the coast (**Fig. 3-9b**). Scaling analysis of the increasing volume transport along the Korean Coast implies an increase of about 0.2 Sv decade^{-1}, assuming that when the northward current is 0.02 m s^{-1} decade^{-1}, the width is 100 km, and the depth is 100 m. The magnitude matches the value shown in Kida et al. (2021), where the volume transport trend measured by the ADCP shows an increase of about 0.11 Sv decade^{-1}.

On the other hand, the coastal branch of the Japan Sea Throughflow along the Japanese coast shows a much weaker increasing trend. The zonal cross-section of the surface geostrophic flow at 131.625 °E (**Fig. 3-9c**) shows a magnitude of less than 0.005 m s^{-1} decade^{-1}, which can only partly explain the cause of the weak SST trend that is observed around the entrance of the Japan Sea.

The increasing trend in surface geostrophic flow also appears around the maximum SST trend patch in the center of the Japan Sea. The geostrophic flow detaches the coastal branch of the Japan Sea Throughflow and accelerates the northward current. The acceleration of the surface geostrophic flow may be an additional factor in generating the maximum patches in addition to that induced by the frontal shift.

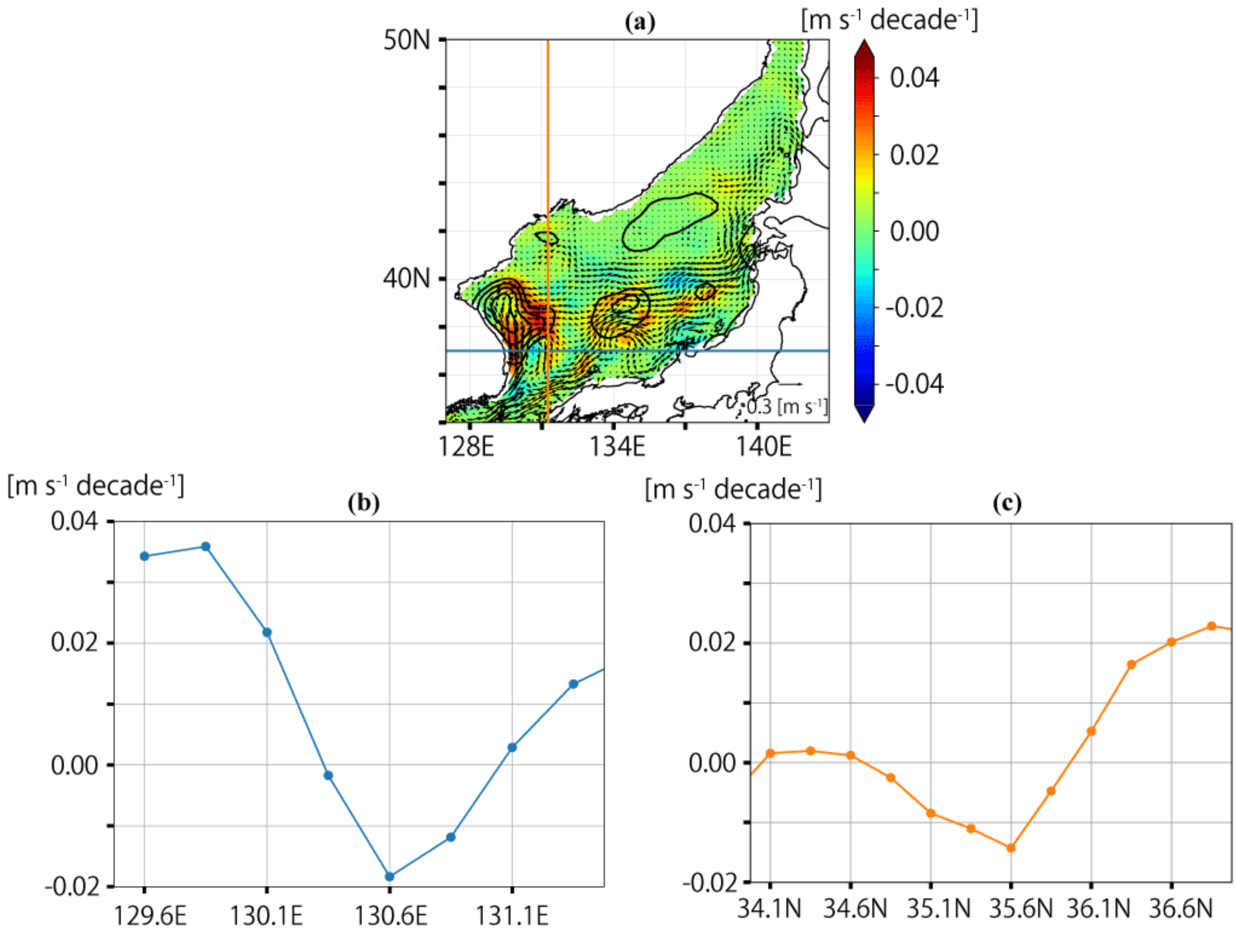

Figure 3-9. (a) Observed current trends from 1993 to 2019. The color shows the current trend, and the black contour shows the magnitude of the SST trend every 0.1 °C $decade^{-1}$ above 0.5 °C $decade^{-1}$. The arrows show the climatological current in the Japan Sea. The horizontal blue and vertical orange lines represent a cross-section of the (b) and (c). (b) shows the current trend along the 37.125 N. (c) shows the current trend along the 131.625E.

3.4 Conclusion

Satellite observations show SST warming trends with maximum and minimum patches within the zonal band structure. Since a strong meridional SST gradient, called the Japan Sea subpolar front, exists in the middle of the Japan Sea. In this chapter, we investigate whether the meridional shift of the SST front can explain the maximum and minimum patches. We also examine how well the shift in the SST front relates to the jet position by estimating its location from sea surface height data.

The meridional shift of the SST front can successfully explain the formation of maximum and minimum patches of SST trend along the SST front. The distribution change from the former period (1993-2002) to the latter period (2010-2019) shows a northward shift of the SST front on the western side and a southward shift in the central and eastern Japan Sea. We also find that the meridional shift of the SST front syncs with the meridional shift of the jet position, suggesting a mechanism of the oceanic current behind the meridional shift of the SST front.

The fronts on the western side gradually shift north for a significant distance of about 0.2 ° decade^{-1}. The fronts on the eastern side gradually shift southward for about 0.1° decade^{-1}. The climatological meridional SST gradient is about 4.0 ℃ 100 km^{-1} so the SST response due to the meridional shifts can explain about 0.8 ℃ decade^{-1} and -0.4 ℃ decade^{-1}, which suggests that the northward and southward shifts of the SST front can be responsible for creating the local maximum and minimum patches along the SST front. However, in the center of the Japan Sea, the SST front and the jet shift south from the former to the latter, which was not well captured by the linear fitting analysis because of the high eddy activity.

Recently, Chen et al. (2022) investigated the decadal movement of the SST front from 1985 to 2020, discovering a gradual southward shift in the central Japan Sea (130-135°E) and a northward shift in the eastern Japan Sea (135-138°E). They suggested a slantwise movement occurred for the long-term shift of the SST front. Our study also observes a similar slantwise movement of the SST front from 1993 to 2019, although we find it to move in the opposite direction. We find a southward shift between 133.125°E-134.875°E (central) and a northward shift between 135.125°E-138.125°E (eastern). This difference is partly attributed to the shorter analysis period in our study compared to that of Chen et al. (2022). According to Figures 3e and 3f in Chen et al. (2022), the southward (northward) SST front movement in the central (eastern) Japan Sea depends on the period before our analysis (1985-1992). Chen et al. (2022) also examined the underlying mechanisms through the front genesis rate equation, identifying the geostrophic zonal advection term as a crucial factor in the decadal position of the central and eastern SST fronts. Their findings for accelerating geostrophic current in the center of the Japan Sea are in line with frequency distribution analysis, which corresponds to the case where the jet position moved southward from the former to the later period, resulting in a new front rather than a gradual shift.

We further find that the northward trend in surface geostrophic current can also explain part of the local maximum patches of the SST trend. Increasing surface geostrophic currents exist along the Korean coast matching the position of the maximum SST trend. The magnitude of this trend is also similar to the observed trend in the flow field across the Tsushima Strait (Kida et al., 2021), suggesting that the strongest SST trend near the Korean coast may be excited by the northward trend and have a connection to the volume transport change across the Tsushima Strait. The trend in the flow field is also observed in the central part of the Japan Sea, where the coastal branch detaches, suggesting the local maximum patch in the central part of the Japan Sea is excited by the acceleration of the northward geostrophic flow.

Chapter 4 Conclusion and Final remarks

4.1 Conclusion

Satellite observations reveal a trend of SST warming over the Japan Sea that is characterized by a meridionally alternating zonal band structure and local maximum and minimum patches within the band. This study examines the mechanisms behind this observed spatial pattern, hypothesizing that (1) the zonal band structure reflects differences in residence time within the Japan Sea created by the Japan Sea Throughflow and that (2) the local maximum and minimum patches result from the northward and southward shifts of the SST front.

In Chapter 2, we find that zonal band structures form due to the Japan Sea Throughflow and spatially uniform atmospheric heating. We used an idealized flat rectangular coastline model to examine the basic heat budget behind the zonal band structures. Heat budget analysis elucidates that while surface heat flux warms the SST, the horizontal heat transport due to the throughflow prevents this warming effect along its pathway. As a result, a weak SST trend appears around the jet, while a strong SST trend appears in the interiors. A realistic coastline model is used to examine the bathymetric effects. The model shows that the separation point of the western boundary current along the coast of Korea stabilizes. On the other hand, the coastal branch begins to detach from the Japanese coastline towards the north. As a result, the SST warming region in the southern interior further stabilizes. Lagrangian analysis using a particle tracking model confirms that a weak SST trend forms where the residence time is short, while a strong SST trend forms where the residence time is long. Resident time is a key parameter that determines the spatial distribution of the long-term SST warming trend and is equivalent to the accumulation time of surface heating. Eddies in the Japan Sea prolong the residence time in interior regions.

In Chapter 3, we analyzed satellite data to identify a northward shift of the SST front on the western side (0.2°decade^{-1}), a southward shift in the central, and a southward shift on the eastern side (0.1° decade^{-1}) of the Japan Sea. The movement of the SST front matched well with that of the jet. Based on a climatological SST gradient of 4.0 ℃ 100 km^{-1} along the front, these shifts explain SST changes of approximately 0.8 ℃ 100 km^{-1} (west) and 0.4 ℃ decade^{-1} (central, east). However, we also found that the movement of the SST front and jets does not necessarily match that based on linear fitting if multiple frontal locations exist. We further find an increasing trend in the northward flow along the Korean coast which can be an additional factor in creating a maximum SST trend.

4.2 Final remarks

Our model experiments simplified various processes to illuminate the role of the throughflow in driving the spatial variability of the SST warming trend. We also examined the impact of the shift in the location of the SST front on the SST warming trend. Here, we discuss how the potential roles of other processes may impact our results and guide future research.

We focused on a scenario where the surface heat flux anomaly always warmed the SST with no time variability. However, surface heat flux can change over time. The net surface heat flux released to the atmosphere has increased over the Japan Sea (Wang et al., 2022). This feature aligns well with Lee and Park (2019), where they find a decline in the SST warming trend. To examine its impact in our model, we need to reduce the magnitude of the surface heat flux anomaly, which we have kept constant. The warming trend will weaken, and SST cooling may occur if Q' becomes negative. It is important to note that the surface heat flux $\bar{Q}$ used in our model is not the long-term average of the observed surface heat flux. It is set to maintain a steady SST in the Japan Sea. Determining the exact $\bar{Q}$ from observations alone is challenging, as it is determined by various factors, such as the strength of the Japan Sea Throughflow. A surface heat flux of about -53 $W\ m^{-2}$ is suggested to balance the Japan Sea Throughflow by Hirose et al. (1996). Recently observed values show much weaker values, consistent with the recent SST warming trend. To evaluate the role of each process in more detail, we will need to use a realistic reanalysis product.

We utilized constant surface heat flux, but seasonal variation may enhance the impact of advection on the SST trend in the interior region. Seasonal heat flux variation can form meridional SST gradient structures in a wide area of the Japan Sea associated with zonal flow (Kim et al., 2020). Zonal advection may increase in the interior of the sea and act to reduce the strength of the SST trend in areas that are not directly along the path of the throughflow, thus weakening the contrast between zonal band structures.

Seasonal variation in the Japan Sea Throughflow volume transport also changes and may affect the SST trend. Seasonal increase in eddy formation is suggested for the southern interior region (Kawabe 1982a; Ito et al., 2014; Yabe et al., 2021). The three maxima of SST observed in the southern half of the Japan Sea may be established due to the contribution of such features. When eddies reside in the area for a long time, residence time increases as demonstrated by the particle tracking model in P-AIR (**Fig. 2-12b**).

Our hypothesis about the Tsushima Warm Current is based on two factors. One is that SST warming is weaker in the Tsushima Strait than in the Japan Sea, which is supported by observations (JMA 2020). Another is that the volume transport of the Tsushima Warm Current remains constant. Monitoring the volume transport of the Tsushima Warm Current has indicated a slightly increasing trend (to 0.11 Sv decade^{-1}). Compared to the mean volume transport, this change is one order of magnitude smaller (Kida et al., 2021). However, change in the velocity field may occur and be responsible for enhancing the warming trend along the eastern coast of Korea. As the SST gradient runs perpendicular to the flow direction, the increase in meridional flow can create an increase in meridional heat transport. The impact of the increase in heat transport along the coast of Japan is likely limited because the flow is more zonally oriented, and the zonal SST gradient is small along the coast of Japan.

Our focus is on the long-term trend in the SST, but these long-term changes in SST trends can have significant consequences on atmospheric events, especially snowfall. Winter snowfall in Japan has been particularly suggested to be affected by changes in SST and its spatial distribution over the Japan Sea (Yamamoto and Hirose 2008; Takahashi et al., 2013). Heavy snowfall often occurs on the northern coast of Japan when the Japan Sea polar air mass convergence zone (JPCZ) develops (Tachibana et al., 2022), and spatial patterns in the SST trend have been observed to coincide with areas where the JPCZ frequently develops. Such a connection between the spatial patterns in the SST and snowfall is a topic for future study.

References

1. Amante, C. and B.W. Eakins, (2009): ETOPO1 1 Arc-Minute Global Relief Model: Procedures, Data Sources and Analysis. NOAA Technical Memorandum NESDIS NGDC-24. National Geophysical Data Center, NOAA.

2. Banzon, V., Smith, T. M., Chin, T. M., Liu, C. and Hankins, W. (2016): A long-term record of blended satellite and in situ sea-surface temperature for climate monitoring, modeling and environmental studies, Earth Syst. Sci. Data, 8, 165-176, https://doi.org/10.5194/essd-8-165-2016

3. Chen, S., Wang, H., Chen, W., Zhang, Y. and Zhang, Y. (2022): Decadal intensified and slantwise Subpolar Front in the Japan/East Sea, Front. Mar. Sci., 9:1039024, https://doi.org/10.3389/fmars.2022.1038024

4. Choi, B.-J., Haidvogel, D. B. and Cho, Y.-K. (2009): Interannual variation of the Polar Front in the Japan/East Sea from summertime hydrography and sea level data, J. Mar. Syst., 78, 351-362, https://doi.org/10.1016/j.jmarsys.2008.11.021

5. Endo, H., Kitoh, A., Mizuta, R. and Ishii, M. (2017): Future Changes in Precipitation Extremes in East Asia and Their Uncertainty Based on Large Ensemble Simulations with a High-Resolution AGCM, SOLA, 13, 7-12, https://doi.org/10.2151/sola.2017-002

6. Fujita, M., Mizuta, R., Ishii, M., Endo, H., Sato, T., Okada, Y., Kawazoe, S., Sugimoto, S., Ishihara, K., and Watanabe, S. (2019): Precipitation Changes in a Climate With 2-K Surface Warming From Large Ensemble Simulations Using 60-km Global and 20-km

Regional Atmospheric Models, Geophys. Res. Lett., 45, 435-442, https://doi.org/10.1029/2018GL079885

7. Fukudome, K.-I., Yoon, J.-H., Ostrovskii, A., Takikawa, T., and Han, I.-S. (2010): Seasonal Volume Transport Variation in the Tsushima Warm Current through the Tsushima Straits from 10 Years of ADCP Observations, J. Oceanogra., 66, 539-551, https://doi.org/10.1007/s10872-010-0045-5

8. Hirose, N., Kim, C.-H., and Yoon, J.-H. (1996): Heat Budget in the Japan Sea. J. Oceanogra., 52 553-574, https://doi.org/10.1007/BF02238321

9. Hogan, P. J. and Hurlburt, H. E. (2000): Impact of Upper Ocean-Topographical Coupling and Isopycnal Outcropping in Japan/East Sea Models with 1/8˚ to 1/64˚ Resolution, J. Phys. Oceanogra., 30(10), 2535-2561, https://doi.org/10.1175/1520-0485(2000)030<2535:IOUOTC>2.0.CO;2

10. Ichie, T. (1984): Some problems of circulation and hydrography of the Japan Sea and the Tsushima Current. Ocean Hydrodynamics of the Japan Sea and East China Seas, T. Ichiya, Ed., Elsevier, 15-54.

11. IPCC (2023): Climate Change 2023: Synthesis Report. Contribution of Working Groups 1, 2, and 3 to the Sixth Assessment Report of the Intergovernmental Panel on Climate Change [Core Writing Team, H. Lee and J. Romero (eds.)]. IPCC, Geneva, Swizerland 35-115, https://doi.org/10.59327/IPCC/AR6-9789291691647

12. Isoda, Y. (1994a): Interannual SST variations to the north and south of the polar front in the Japan Sea, La Mer, 32, 285-293

13. Isoda, Y. (1994b): Warm Eddy Movements in the Eastern Japan Sea, J. Oceanogra., 50, 1-15 https://doi.org/10.1007/BF02233852

14. Ito, M., Morimoto, A., Watanabe, T., Katoh, O. and Takikawa, T. (2014): Tsushima Warm Current paths in the southwestern part of the Japan Sea, Prog. Oceanogra., 121, 83-93, https://doi.org/10.1016/j.pocean.2013.10.007

15. Japan Meteorological Agency (2020): Climate Change in Japan Report on Assessment of Observed/Projected Climate Change Relating to the Atmosphere, Land and Oceans. https://www.data.jma.go.jp/cpdinfo/ccj/index.html, Accessed 8 September 2023

16. Kawabe, M. (1982a): Branching of the Tsushima Current in the Japan Sea Part 1. Data Analysis. J. Oceanogra. Soc. Jpn., 38 95-107, https://doi.org/10.1007/BF02110295

17. Kawabe, M. (1982b): Branching of the Tsushima Current in the Japan Sea Part 2. Numerical Experiment., J. Oceanogra, Soc. Jpn., 38, 183-192, https://doi.org/10.1007/BF02111101

18. Kawase, H., Murata, A., Mizuta, R., Sasaki, H., Nosaka, M. Ishii, M. and Takayabu, I. (2016): Enhancement of heavy daily snowfall in central Japan due to global warming as projected by large ensemble of regional climate simulations, Climatic Change, 139, 265-278, https://doi.org/10.1007/s10584-016-1781-3

19. Kawase, H. Fukui, S., Nosak, M. Watanabe, S. I., Otomo, K., Murata, A., Murazaki, K. and Nakaegawa, T. (2023): Historical regional climate changes in Japan in winter as assessed by a 5-km regional climate model with a land surface process, Prog Earth Planet Sci, 10, 7, https://doi.org/10.1186/s40645-023-00536-4

20. Kida, S., Mitsudeara, H. Aoki, S., Guo, X., Ito, S., Kobashi, F., Komori, N., Kubokawa, A., Miyama, T., Morie, R., Nakamura, H., Nakamura, T., Nakano, H., Nishigaki, H., Nonaka, M., Sasaki, H., Sasaki, Y., N., Suga, T., Sugimoto, S., Taguchi, B., Takaya, K., Tozuka, T., Tsujino, H., Usui, N. (2015): Oceanic fronts and jets around Japan: a review, J. Oceanogr., 71, 469-497, https://doi.org/10.1007/s10872-015-0283-7

21. Kida, S., Qiu, B. Yang, J., and Lin, X. (2016): The Annual Cycle of the Japan Sea Throughflow. J. Phys. Oceanogr., 46, 23-39, https://doi.org/10.1175/JPO-D-15-0075.1

22. Kida, S., Takayama, K., Sasaki, Y. N., Matsuura, H. and Hirose, N. (2021): Increasing trend in Japan Sea Throughflow transport, J. Oceanogr., 77, 145-153, https://doi.org/10.1007/s10872-020-00563-5

23. Kim, D., Shin. H.-R., Kim, C.-H. and Hirose, N. (2020): Characteristics of the East Sea (Japan Sea) circulation depending on surface heat flux and its effect on branching of the Tsushima Warm Current, Cont. Shelf Res., 192, 104025, https://doi.org/10.1016/j.csr.2019.104025

24. Kodama, T., Igeta, Y., Kuga, M., and Abe, S. (2016): Long-term decrease in phosphate concentrations in the surface layer of the southern Japan Sea, J. Geophys. Res. Oceans, 121, 7845-7856, https://doi.org./10.1002/2016JC012168

25. Kuroda, H., Saito T., Kaga, T., Takasuka, A., Kamimura, Y., Furuishi, S. and Nakanowatari, T. (2020): Unconventional Sea Surface JTemperature Regime Around Japan in the 2000s-2010s: Potential Influences on Major Fisheries Resources., Front. Mar. Sci., 7:574904, https://doi.org/10.3389/fmars.2020.574904

26. Lee, E.-Y. and Park, K.-A. (2019): Change in the Recent Warming Trend of Sea Surface Temperature in the East Sea (Sea of Japan) over Decades (1982-2018). Remote Sens. 11(22), 2613, https://doi.org/10.3390/rs11222613

27. Locarnini, R. A., A. V. Mishonov, O. K. Baranova, T. P. Boyer, M. M. Zweng, H. E. Garcia, J. R. Reagan, D. Seidov, K. W. Weathers, C. R. Paver, I. V. Smolyar, 2019: World Ocean Atlas 2018, Volume 1: Temperature. A. V. Mishonov, Technical Ed., NOAA Atlas NESDIS 81.

28. Matsumura, Y. and Hasumi, H. (2008): A non-hydrostatic ocean model with a scalable multigrid Poisson solver. Ocean Modell., 24, 15-28, https://doi.org/10.1016/j.ocemod.2008.05.001

29. Matsuura, H. and Kida, S. (2024): Role of Japan Sea Throughflow in the spatial variability of the long-term sea surface temperature trend. J. Oceanogr., 80, 291-307, https://doi.org/10.1007/s10872-024-00723-x

30. Minobe, S., Sako, A., and Nakamura, M. (2004): Interannual to Interdecadal Variability in the Japan Sea Based on a New Gridded Upper Water Temperature Dataset. J. Phys. Oceanogr, 34, 2383-2397, https://doi.org/10.1175/JPO2627.1

31. Nosaka, M., Ishii, M., Shiogama, H., Mizuta, R., Murata, A., Kawase, H. and Sasaki, H. (2020): Scalability of future climate changes across Japan examined with large-ensemble simulations at + 1.5K, +2K, and +4K global warming levels, Prog. Earth Planet Sci. (2020), https://doi.org/10.1186/s40645-020-00341-3

32. Ohishi, S., Aiki, H., Tozuka, T. and Cronin, M. F. (2019): Frontolysis by surface heat flux in the eastern Japan Sea: importance of mixed layer depth, J. Oceanogr., 75, 283-297, https://doi.org/10.1007/s10872-018-0502-0

33. Park, K.-A., Chung, J. Y., and Kim, K. (2004): Sea surface temperature fronts in the East (Japan) Sea and temporal variations. Geophys. Res. Lett., 31(7), L07304, https://doi.org/10.1029/2004GL019424

34. Park, K.-A., Ullman, D. S., Kim, K., Chung. J. Y., and Kim, K. R. (2007): Spatial and temporal variability of satellite-observed Subpolar Front in the East/Japan Sea, Deep Sea Res. I, 54, 453-470, https://doi.org/10.1016/j.dsr.2006.12.010

35. Shiogama, H., Imada, Y., Mori, M., Mizuta, R., Stone, D., Yoshida, K. Arakawa, O., Ikeada, M., Takahashi, C., Arai, M., Ishii, M., Watanabe, M. and Kimoto, M. (2016): Attribution Historical Changes in Probabilities of Record-Breaking Daily Temperature and Precipitation Extreme Events, SOLA, 12, 225-231, https://doi.org/10.2151/sola.2016-045

36. Tachibana, Y., Honda, M., Nishikawa, H. et al. (2022): High moisture confluence in Japan Sea polar air mass convergence zone captured by hourly radiosonde launches from a ship. Sci. Rep., 12, 21674, https://doi.org/10.1038/s41598-022-23371-x

37. Takahashi, H. G., Ishizaki, N. N., Kawase, H., Hara, M., Yoshikane, T. Ma, X. and Kimura, F. (2013): Potential Impact of Sea Surface Temperature on Winter Precipitation over the Japan Sea Side of Japan: A Regional Climate Modeling Study, J. Meteor. Soc. Japan, 91, 471-488, https://doi.org/10.2151/jmsj.2013-404

38. Takikawa, T., Yoon, J.-H., and Cho, K-D. (2004): The Tsushima Warm Current through Tsushima Stratis Estimated from Ferryboat ADCP Data, J. Phys. Oceanogr., 35, 1154-1168, https://doi.org/10.1175/JPO2742.1

39. Taguchi, B., Schneider, N., Nonaka, M. and Sasaki, H. (2017): Decadal Variability of Upper-Ocean Heat Content Associated with Meridional Shifts of Western Boundary Current Extensions in the North Pacific. J. Clim., 30-16, 6247-6264, https://doi.org/10.1175/JCLI-D-16-0779.1

40. Tomita, H., Hirata, T., Kako, S. Kubota, M., and Kutsuwada, K. (2019): An introduction to J-OFURO3, a third-generation Japanese ocean flux data set using remote-sensing observations, J. Oceanogr., 75, 171-194, https://doi.org/10.1007/s10872-018-0493-x

41. Umlauf, L. and Burchard, H. (2003): A generic length-scale equation for geophysical turbulence models, J. Marine Res., 61, 235-265, https://elischolar.library.yale.edu/journal_of_marine_research/9

42. Watanabe, T., Hanawa, K., and Yoba, Y. (1986): Analysis of year-to-year variation of water temperature along the coast of the Japan Sea. Prog. in Oceanogr., 17, 337-357, https://doi.org/10.1016/0079-6611(86)90053-4

43. Wang, D., Xu, T., Fang, G., Jian, S., Wang, G., Wei, Z and Wang, Y. (2022): Characteristics of Marine Heatwaves in the Japan/East Sea. Remote Sens., 14(4), 936, https://doi.org/10.3390/rs14040936

44. Wu, Z. Jiang, C., Conde, M., Chean, J. and Deng, B. (2020): The long-term spatiotemporal variability of sea surface temperature in the northwest Pacific and China offshore. Ocean Sci., 16, 83-97, https://doi.org/10.5194/os-16-83-2020

45. Yabe, I., Kawaguchi, Y., Wagawa, T. and Fujio, S. (2021): Anatomical study of Tsushima Warm Current system: Determination of Principal Pathways and its Variation. Prog. Oceanogr., 194, 102590, https://doi.org/10.1016/j.pocean.2021.102590

46. Yamamoto, M. and Hirose, N. (2008): Influence of assimilated SST on regional atmospheric simulation: A case of a cold-air outbreak over the Japan Sea, Atmos. Sci. Let., 9, 13-17, https://doi.org/10.1002/asl.164

47. Yeh, S.-W., Park, Y.-G., Min, H., Kim, C.-H. and Lee, J-H. (2010): Analysis of characteristics in the sea surface temperature variability in the East/Japan Sea, Prog. Oceanogra., 121, 83-93, https://doi.org/10.1016/j.pocean.2013.10.007

48. Yoon, J. H. (1982): Numerical Experiment on the Circulation in the Japan Sea Part III. Mechanism of the Nearshore Branch of the Tsushima Current., J. Oceanogr. Soc. Jpn., 38, 125-130, https://doi.org/10.1007/BF02110283

49. Yoon, J.-H., Abe, K., Ogata, T. and Wakamatsu, Y. (2005): The effects of wind-stress curl on the Japan/East Sea circulation, Deep Sea Res. II, 52, 1827-1844, https://doi.org/10.1016/j.dsr2.2004.03.004

50. Yoshida, K. Sugi, M., Mizuta, R. Murakami, H. and Ishii, M. (2017): Future Changes in Tropical Cyclone Activity in High-Resolution Large-Ensemble Simulations, Geophys. Res. Lett., 44, 9910-9917, https://doi.org/10.1002/2017GL075058

51. Zhao, N., Iwasaki, S., Isobe, A., Lien, R.-C. and Wang, B. (2017): Intensification of the subpolar front in the Sea of Japan during winter cyclones, J. Geophys. Res. Oceans, 121, 2253-2267, https://doi.org/10.1002/2015JC011565

Appendix

The distribution of the SST front from 1993 to 2019

Zone1 [129.125°E ~ 129.825°E]:

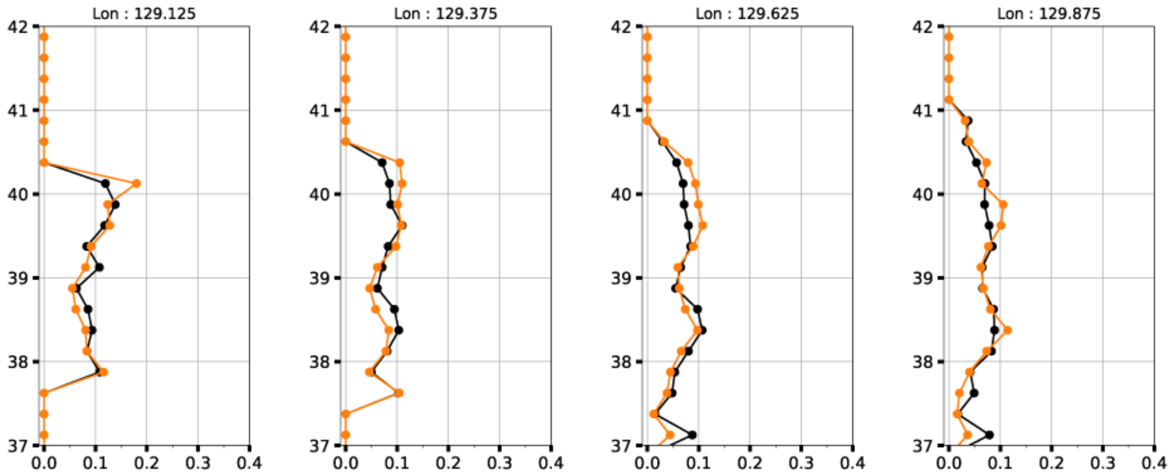

Zone2 [133.125°E ~ 134.875°E]:

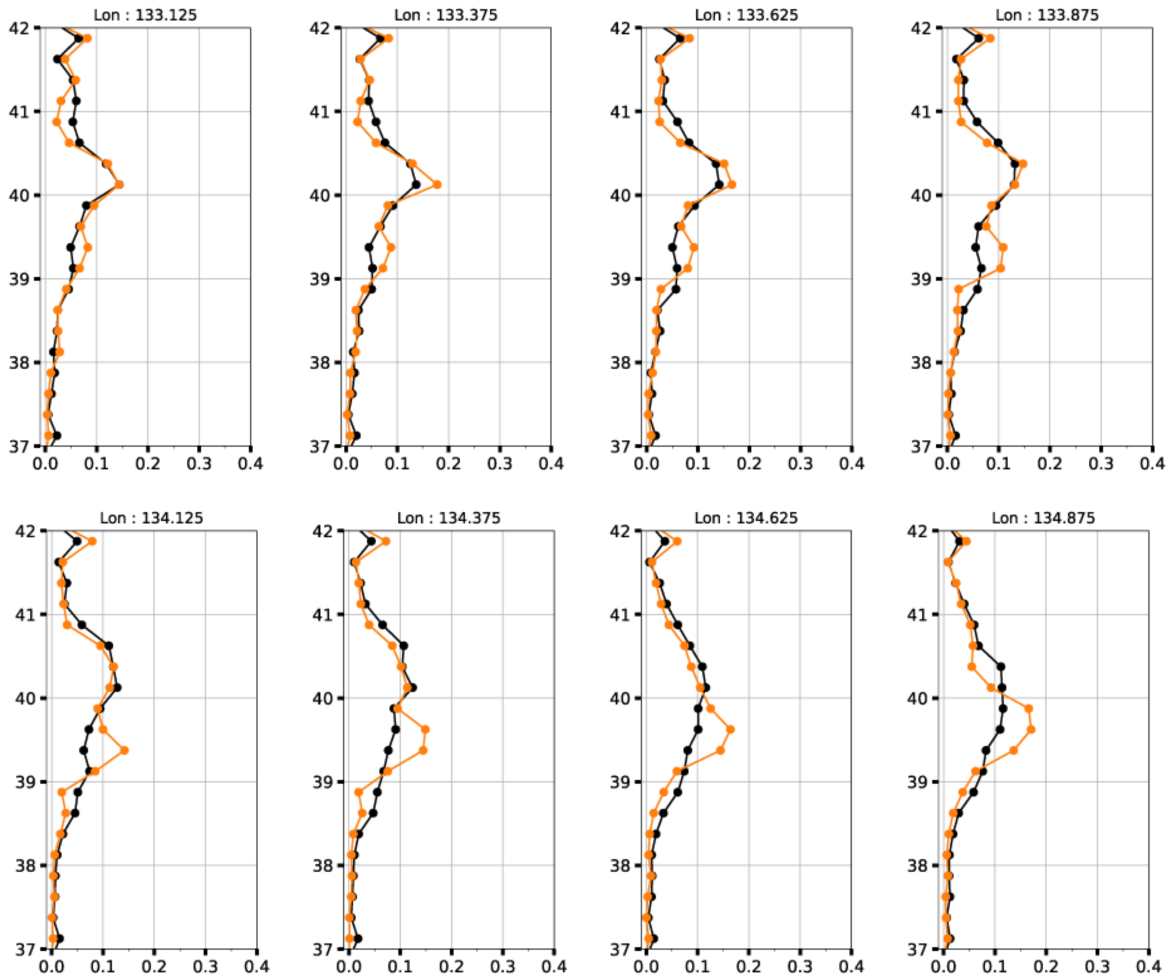

Zone3 [135.125°E ~ 138.125°E]:

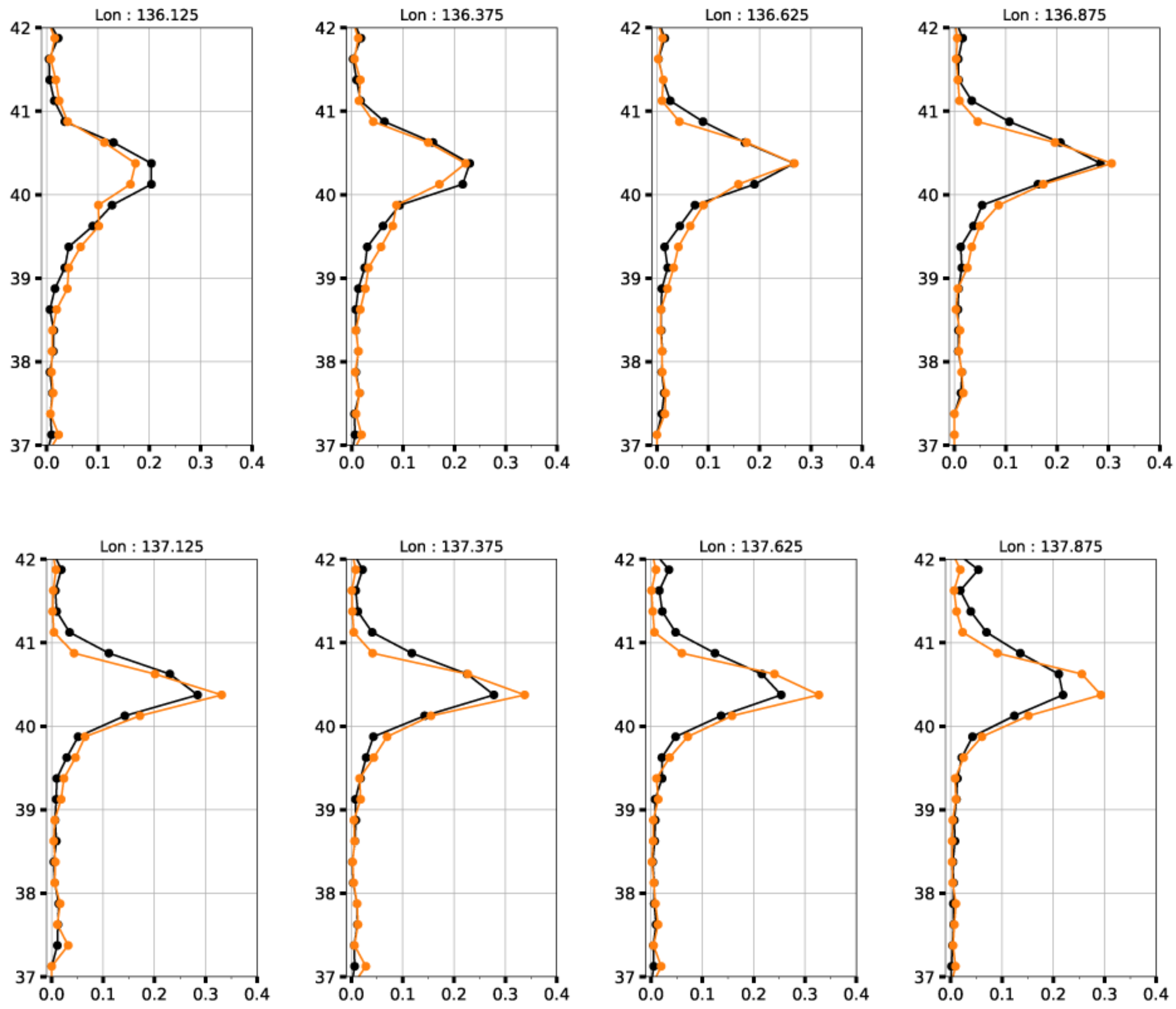

The distribution of the jet from 1993 to 2019

Zone1 [129.125~ 129.825°E]:

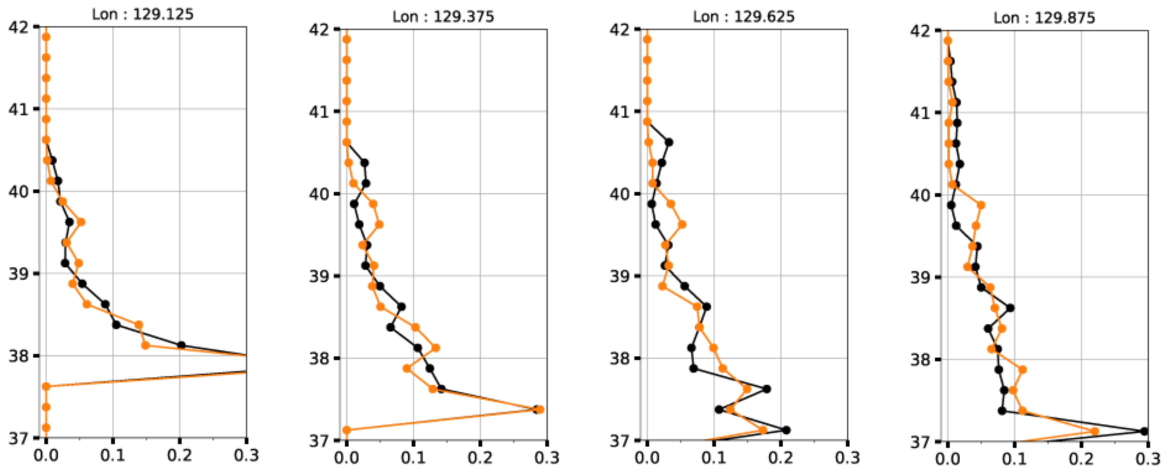

Zone2 [133.125°E ~ 134.875°E]:

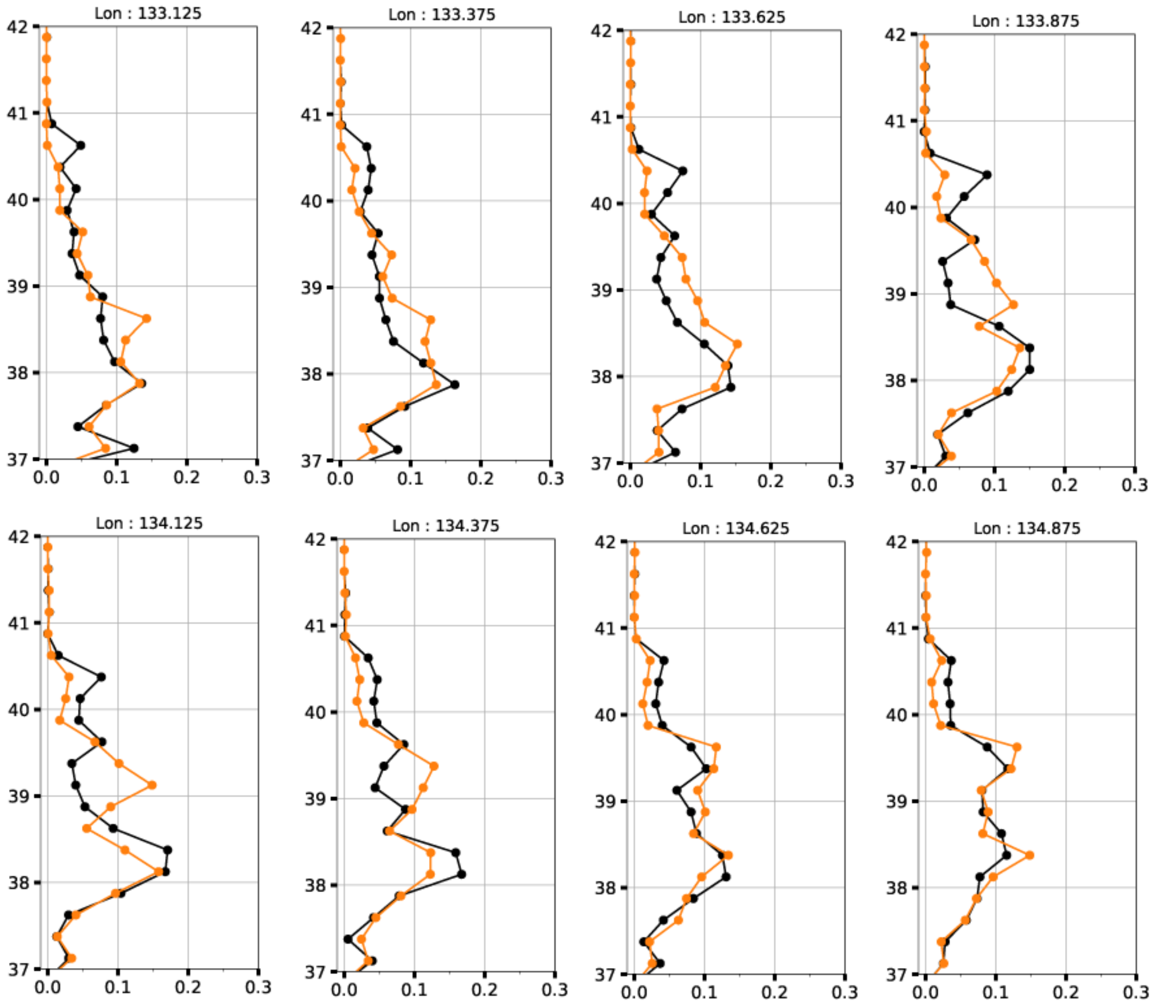

Zone3 [135.125°E ~ 138.125°E]: